TEL AVIV UNIVERSITY
RAYMOND AND BEVERLY SACKLER
FACULTY OF EXACT SCIENCES

Energy dependence of $\sigma_{\mathrm{tot}}(\gamma p)$ measured with the ZEUS detector at HERA

Thesis submitted toward the M.Sc. Degree
at Tel Aviv University
School of Physics and Astronomy

by

Orel Gueta

July 30, 2010

The research work for this thesis was carried out in the Experimental High Energy Physics Group of the Tel Aviv University under the supervision of Prof. **Halina Abramowicz** and Prof. **Aharon Levy**.

To my parents,
Esther and Gedeon.

Abstract

The energy dependence of the total photon-proton cross-section is determined using data collected at three different proton beam energies with the ZEUS detector at HERA.

Contents

Chapter 1

Introduction

The energy dependence of photon-proton total cross section is an important measurement that allows to predict the energy dependence of hadron-hadron total cross sections and to provide a test to its asymptotic behavior. Past measurements of hadron-hadron and photon-hadron cross sections are available at low energies [1] and at high energies with large systematic uncertainties [2,3,4]. The latter confirmed the expected rise of the total γp cross section with energy. However, such uncertainties do not yet allow discrimination between different models predicting a moderate rise of the γp total cross section [4]. Measuring the total γp cross section at three different energies enables a direct determination of the energy dependence.

Adopting Regge theory, Donnachie and Landshoff (DL) [5] parameterized the energy dependence of all hadron-hadron (h-h) total cross sections using the form

$$\sigma_{\text{tot}}^{\text{h-h}} = A(W^2)^{\epsilon} + B(W^2)^{-\eta}, \tag{1.1}$$

where W is the center-of-mass energy and A and B are constants. The parameters $\alpha_{I\!P}(0) = 1 + \epsilon$ and $\alpha_{I\!R}(0) = 1 - \eta$ denote the intercepts of the Pomeron and the Reggeon trajectories, respectively. Donnachie and Landshoff fitted the energy dependence of a number of hadronic total cross sections and found $\epsilon = 0.0808$ and $\eta = 0.4525$ (see Fig. 1.1). Further measurements [6,7] yielded $0.08 < \epsilon < 0.10$ as an acceptable range of intercepts for the Pomeron trajectory.

The ep collider HERA, with $W \approx 318$ GeV, opens up the possibility to measure the total photon-proton cross section, $\sigma_{\text{tot}}(\gamma p)$, at high energies.

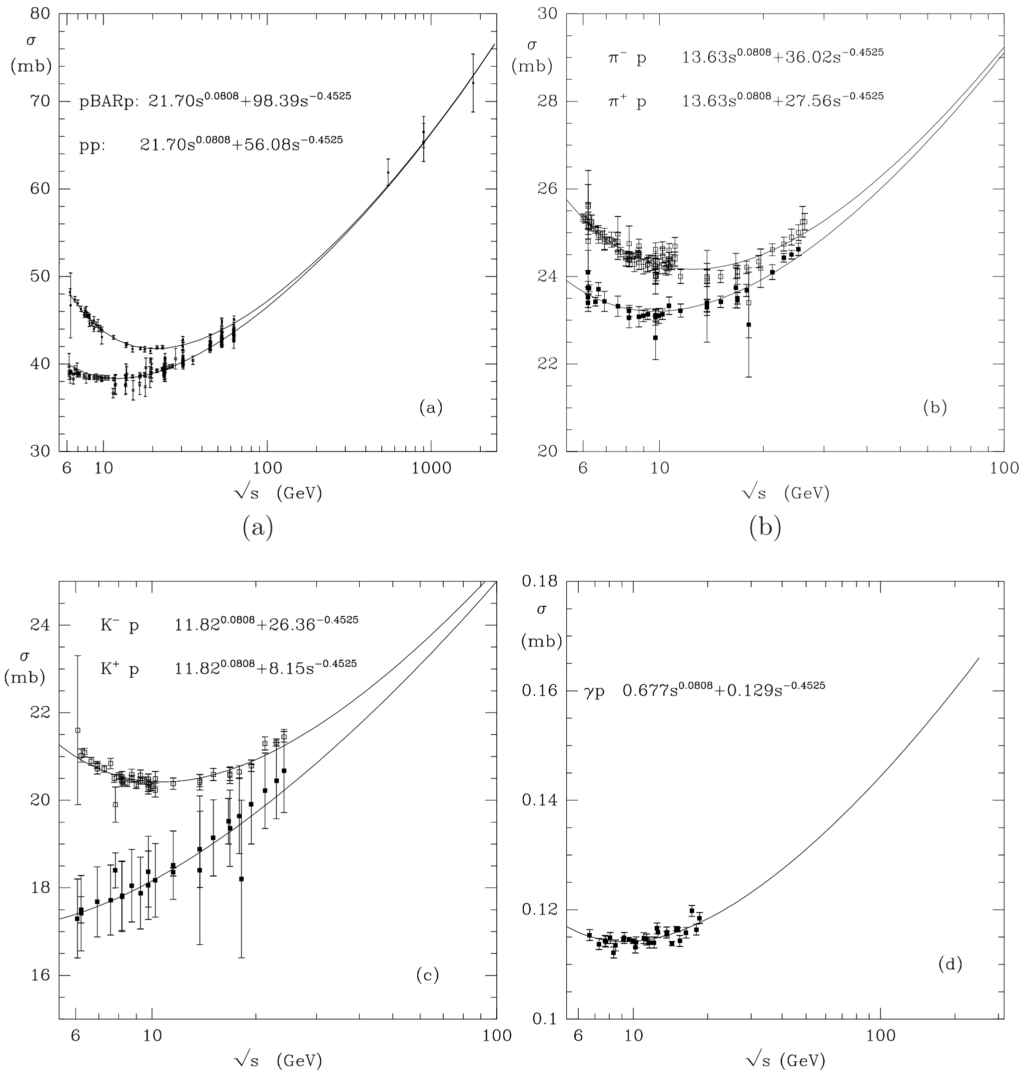

(a) (b)

(c) (d)

Figure 1.1: The total cross section, σ, as a function of center of mass energy, $\sqrt{s}$, for (a) pp, $\bar{p}p$ (b) π^+p , π^-p (c) K^+p, K^-p (d) γp. The lines show the DL parametrization.

Taking events with very low momentum transferred squared ($Q^2 \simeq 0$ GeV^2), one can extract $\sigma_{\text{tot}}(\gamma p)$ from $\sigma_{\text{tot}}(e^+p)$. These events, $e^+p \to e^+X$ with $Q^2 \simeq 0$ GeV^2, are called photoproduction events.

Measuring cross sections in a collider environment requires a very accurate measurement of the acceptance of the detector. This is particularly hard for processes such as photoproduction, where some of the final state particles are anticipated to disappear down the beam-pipe. The acceptance is then calculated using a Monte-Carlo simulation, which in turn introduces a large systematic uncertainty in the final result.
By measuring the ratio of cross sections at different center-of-mass energies with a single detector, such systematic uncertainties are expected to cancel out. Moreover, measuring such a ratio allows to directly probe the power of the W dependence.

The last runs of HERA were taken with three different proton energies at constant positron energy. At constant positron energy, the flux of virtual photons is independent of the proton energy and $\sigma^{e^+p} \sim \sigma_{\text{tot}}(\gamma p)$. Therefore, the ratio $r_{1,2}$ of e^+p cross sections at different center of mass energies is equal to the ratio of γp cross sections. Assuming $\sigma_{\text{tot}}(\gamma p) \sim W^\delta$, one can calculate the ratio

$$r_{1,2} = \frac{\sigma^{e^+p}(W_1)}{\sigma^{e^+p}(W_2)} = \left(\frac{W_1}{W_2}\right)^\delta, \tag{1.2}$$

where the index 1(2) denotes the measurement performed at W_1 (W_2). Experimentally,

$$\sigma^{e^+p} = \frac{N}{A \cdot \mathcal{L}}, \tag{1.3}$$

where N, A and $\mathcal{L}$ are the number of measured events, the acceptance and the luminosity, respectively. The ratio $r_{1,2}$ is then given by

$$r_{1,2} = \frac{N_1}{N_2} \cdot \frac{A_2}{A_1} \cdot \frac{\mathcal{L}_2}{\mathcal{L}_1}. \tag{1.4}$$

Integrating the third measurement is then natural,

$$R \equiv r_{1,2} \cdot r_{1,3} = \frac{N_1^2}{N_2 N_3} \cdot \frac{A_2 A_3}{A_1^2} \cdot \frac{\mathcal{L}_2 \mathcal{L}_3}{\mathcal{L}_1^2} = \left(\frac{W_1^2}{W_2 \cdot W_3}\right)^\delta. \tag{1.5}$$

Given that the change in W results from changing the proton energy, and that the trigger is based on the energy flow in the positron direction (rear), it is reasonable to assume that the trigger acceptance is independent of W and to drop the ratio of acceptances in Eq. (1.5).

The aim of this analysis is to evaluate ϵ by measuring the ratio R and using the relation $\delta = 2\epsilon$.

This dissertation includes a description of the HERA accelerator and the ZEUS detector (chapter 2), a theoretical overview of the photoproduction process and the techniques used to measure it (chapter 3), a description of the event selection procedure (chapter 4), and finally, the extraction of the value of ϵ (chapter 5).

Chapter 2

Experimental Setup

2.1 The HERA accelerator

The Hadron-Electron Ring Accelerator HERA was a lepton-proton collider at the Deutsche Elektronen Synchrotron DESY in Hamburg, which operated from October 19, 1991 to June 30, 2007. The machine functioned with electrons of nominal energy 27.5 GeV and protons of nominal energy 920 GeV, leading to a center-of-mass energy of $\approx$ 318 GeV. Protons and electrons travelled in bunches separated by about 29 m, corresponding to 96 ns. Some of the bunches, referred to as pilot bunches, had no corresponding bunch in the other beam. These pilot bunches were used for background studies.

HERA underwent a major luminosity upgrade during a shut-down which began in 2000 [8].

In the last months of its physics program, HERA was operated at different center of mass energies. The proton energy was decreased to 460 GeV from March 26 to June 1, 2007, referred to as low energy run period (LER), and to 575 GeV from June 1 to June 30, 2007, referred to as medium energy run period (MER). The time span before March 26, 2007 during which HERA was run with a proton energy of 920 GeV is referred to as high energy run period (HER). In all periods, the positron energy remained at 27.5 GeV.

2.2 The ZEUS detector

The ZEUS detector [9,10] was a multi-purpose detector located in the south hall of HERA. The detector covered almost the full solid angle around the interaction point (IP) in order to detect high energy particles in *ep* interactions. The detector components used in this analysis are: the main calorimeter (CAL), the central tracking detector (CTD), the six meter tagger (6mT) and the luminosity monitoring system (LUMI).

The ZEUS coordinate system is a right-handed Cartesian system with the z axis pointing in the proton beam direction, referred to as "forward direction", and the x axis pointing towards the centre of HERA. The coordinate origin is at the nominal interaction point.

2.2.1 The main calorimeter

The high-resolution uranium-scintillator calorimeter [11] consisted of three parts: the forward (FCAL), the barrel (BCAL) and the rear (RCAL) calorimeters. Each part was subdivided transversely into towers and longitudinally into one electromagnetic section (EMC) and either one (in RCAL) or two (in BCAL and FCAL) hadronic sections (HAC). Typical tower sizes were 20×20 cm^2 in the hadronic section and 5×20 cm^2 (10×20 cm^2 in RCAL) in the electromagnetic section. The smallest subdivision of the calorimeter was called a cell. The CAL energy resolutions, as measured under test-beam conditions, were $\sigma(E)/E = 0.18/\sqrt{E}$ for electrons and $\sigma(E)/E = 0.35/\sqrt{E}$ for hadrons, with E in GeV.

2.2.2 The Central Tracking Detector

Charged particles were tracked in the central tracking detector [12] and in the microvertex detector (MVD) [13]. These components operated in a magnetic field of 1.43T provided by a thin superconducting solenoid. The CTD drift chamber, consisting of 72 sense wire layers organised into 9 super layers, provided a relative resolution of the transverse momentum of $\sigma(P_t)/P_t = 0.0058P_t \oplus 0.0014/P_t$ with P_t in GeV. This corresponds to a resolution of about 1 cm for vertex positions reconstructed from hits in the CTD. Tracks reconstructed from hits in the MVD had vertex position resolutions of a few μm.

2.2.3 The luminosity system

Luminosity is a key quantity when measuring cross sections in collider experiments. The ZEUS experiment employed the precisely calculable Bethe-

Heitler (BH) process, $e^+p \to e^+\gamma p$, to determine the luminosity. The theoretical value of the cross section, known within 0.5% [14], combined with the number of BH events registered in the luminosity detector, allowed to measure the luminosity according to the relation

$$\mathcal{L} = \frac{N_{\mathrm{BH}}}{A_{\mathrm{BH}} \cdot \sigma_{\mathrm{BH}}}, \tag{2.1}$$

where N_{BH}, A_{BH} and σ_{BH} denote the number of events, the acceptance and the cross section respectively.

The photon and the positron from a Bethe-Heitler process occurring inside the ZEUS detector were generally radiated at very small angles with respect to the direction of the incoming positron. Therefore, both the positron and the photon left the detector through the beam-pipe in the direction of the positron beam. The photon, unaffected by magnetic fields, traveled straight down the beam-pipe and left it through an exit window located 92 m behind the nominal interaction point. The energy of the photon was measured by two independent systems, the photon calorimeter (PCAL), installed 107 m from the interaction point, and the spectrometer [15]. The positron was bent by dipole magnets towards the 6 meter tagger described in Sect. 2.2.4. The 6mT was used as a tool to calibrate the PCAL and cross check its acceptance [16]. A schematic view of the ZEUS luminosity measurement system is shown in Fig. 2.1.

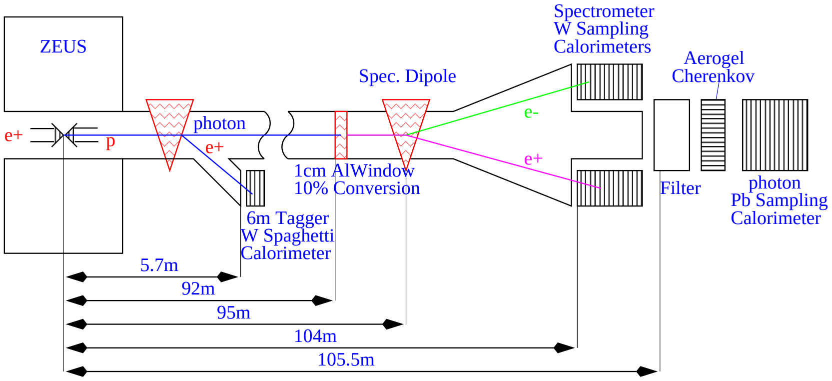

Figure 2.1: Schematic view of the ZEUS luminosity monitor system, consisting of an electron tagger, a pair spectrometer, and a photon calorimeter with an active filter.

It was necessary to use two separate systems to measure luminosity after the HERA upgrade in order to meet the required accuracy because of two major problems,

- significant increase in synchrotron radiation;
- increase in the number of BH overlayed events (pile-up) to 1.3-1.5 per HERA bunch crossing.

The PCAL was a lead-scintillator sampling calorimeter with a depth of $24X_0$, read out by two photomultipliers. The PCAL was shielded against synchrotron radiation by an active filter system consisting of two carbon absorbers, each with a depth of $2X_0$, alternating with AEROGEL Cerenkov detectors [17]. The absorbers protect the calorimeter from radiation damage, while the AEROGEL detectors detect high-energy photons that convert in the absorbers, allowing the calorimeter energy to be corrected and good resolution to be recovered [18].

The main advantage of the use of the silica AEROGEL as the Cherenkov radiators is that it is completely 'blind' to synchrotron radiation. This is due to its low refraction index of 1.030 which corresponds to Cherenkov energy threshold for electrons of 1.62 MeV. In case of the ZEUS experiment, the synchrotron radiation penetrating the filter had the critical energy of about 140 keV and its spectrum extended up to 1-2 MeV. Therefore, only a small fraction of photons could give rise to a signal via the Compton Effect. On the other hand, the high energy BH photons generate electromagnetic cascades in the filter. The typical energy of the shower particles is about 20 MeV, much above the silica AEROGEL Cherenkov threshold. Thus, bremsstrahlung photons in the filter could easily be detected [19].

The spectrometer was situated downstream of an exit window composed of an alloy made mainly of aluminum and silicon with a thickness of about 1 cm, corresponding to around 12% of radiation length. Hence, about 8.9% of the traversing BH photons with energies larger than ≈ 1 MeV converted into electron-positron pairs. The electron-positron pairs were separated by a dipole magnet and detected in a pair of tungsten-scintillator sandwich calorimeters, placed above and below the beam-pipe, thus avoiding exposure to synchrotron radiation. In addition, the low acceptance of the spectrometer, due to the exit window, assisted in dealing with pile up events [18, 20].

Using both the PCAL and the spectrometer yielded a luminosity measurement with relative uncertainty of the order of 1.1% [14].

2.2.4 The six meter tagger

The six meter tagger was a $84\times23.4\times100$ mm^3 tungsten-scintillator spaghetti type calorimeter situated 5.7 m from the interaction point in the backward direction (see Fig. 2.1) [21]. It consisted of 70 cells ordered in 5 rows and 14 columns as shown in Fig. 2.2, each cell was of size 6×4.68 mm^2. The radiation length of the 6mT was 3.651 mm and it had a Molière radius (R_{M}) of 7.089 mm [20]. The 6mT was located in a magnetic field 40 cm from an exit window in the beam-pipe which allowed low-angle scattered positrons to hit the tagger. The bending power of the dipole magnets was such that positrons with energies between 4-8 GeV, originating for instance in a BH or photoproduction process, were deflected out of the nominal beam orbit and hit the 6mT [16]. Another feature of the dipole magnets was that they focused the positrons horizontally.

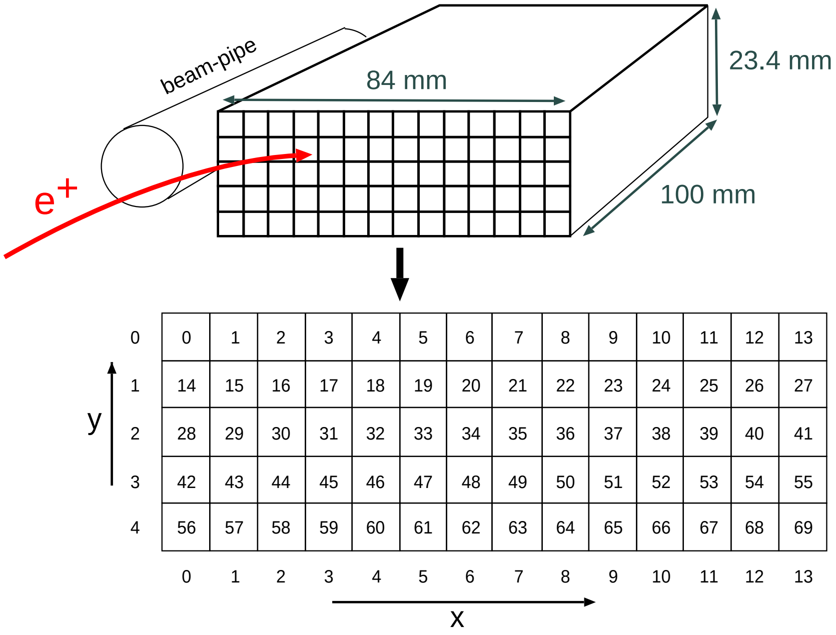

	0	1	2	3	4	5	6	7	8	9	10	11	12	13
0	0	1	2	3	4	5	6	7	8	9	10	11	12	13
1	14	15	16	17	18	19	20	21	22	23	24	25	26	27
2	28	29	30	31	32	33	34	35	36	37	38	39	40	41
3	42	43	44	45	46	47	48	49	50	51	52	53	54	55
4	56	57	58	59	60	61	62	63	64	65	66	67	68	69

Figure 2.2: Schematic view of the 6mT and its cell configuration.

2.2.5 The trigger system

ZEUS used a 3-level trigger system to cope with the high interaction rate of HERA and to reduce the trigger rate to a few Hz [22, 10].
The First-Level Trigger (FLT) had the task to set the trigger rate to 1 KHz by eliminating most of the beam-gas background. Each component in the detector carried out its internal trigger calculations and passed the information of a particular crossing to the global first level trigger (GFLT). Additional processing of calorimeter trigger data was performed by the Fast Clear (FC) between arrivals of global first level triggers. The Fast Clear aborted events before processing by the second level trigger.

Events not rejected by the GFLT and FC were transferred to buffers for processing by the second level trigger (SLT). At the second level the available data is more precise and complete. Therefore, the data from different components can be correlated more accurately, e.g. tracking of charged particles, vertex position determination, muon, jet and electron finding. This enabled the SLT to achieve a reduction of the FLT rate from 1 KHz to 100 Hz.

The data passing the SLT was then sent to the third level trigger (TLT) running on a computer farm. The TLT ran a reduced version of the full offline analysis code and had an output rate of about 3-5 Hz.

Chapter 3

Methodology

3.1 Photoproduction

At HERA, the process $e^+p \rightarrow e^+X$ with $Q^2 \simeq 0$ GeV^2, enables the investigation of interactions between almost real photons and protons at high energies. Typical of strong interactions, the process can be separated into low p_{T} interactions (soft) and high p_{T} interactions (hard).

3.1.1 Soft interactions

The model best describing the photon behaviour in soft interactions is called Vector Meson Dominance (VDM) [23, 24, 25, 26].
The similarity between the hadronic final states in γp interactions and hadron-hadron interactions led to the phenomenological model, in which the photon is considered to be a superposition of the bare photon and a light vector meson (ρ^0, ω or ϕ). It is believed that in high energy interactions, the photon first converts into a vector meson (predominantly the ρ^0) which then interacts with the proton. Hence the name VDM. In the realm of VDM, the bare photon accounts for a small, or perhaps negligible, portion of the interaction.
The following processes contribute to soft photoproduction interactions [3, 27]:

- elastic: $\gamma p \rightarrow Vp$, where V is one of the vector mesons ρ^0, ω or ϕ;
- proton dissociative: $\gamma p \rightarrow VX$, where X is a hadronic state into which the proton diffractively dissociates;

- photon dissociative: $\gamma p \rightarrow Xp$, where X is a hadronic state into which the photon diffractively dissociates;
- double dissociative: $\gamma p \rightarrow X_1 X_2$, where the photon dissociates into the system X_1 and the proton - into X_2;
- soft non-diffractive: where both the proton and the photon lose their identity and the products of the interaction fill up the rapidity space between them.

3.1.2 Hard interactions

Hard interactions are split into reactions of a direct photon and a resolved photon [28]. In the direct photon reaction, the photon interacts directly and all of its energy participates in the hard interaction. In the resolved photon reaction, the interaction can be described as a two-step process in which the photon first resolves into partons and then one of the partons participates in the hard interaction. The direct and resolved photon interactions are subdivided as follows:

- direct:
  - $\gamma q \rightarrow qg$
  - $\gamma g \rightarrow q\bar{q}$.
- resolved:
  - $qq \rightarrow qq$
  - $qg \rightarrow qg$
  - $gg \rightarrow gg$;

3.2 Kinematic Variables

The kinematics of interactions at HERA can be described by the following variables:

- $Q^2 \equiv -q^2 = -(k - k')^2$, the negative four-momentum squared of the virtual photon, where k (k') is the four-momentum of the incident (scattered) positron;

- $W^2 = (q+p)^2$, the squared centre-of-mass energy of the photon-proton system, where p is the four-momentum of the incident proton;
- $y = \frac{p \cdot q}{p \cdot k}$, the fraction of the incoming positron energy carried by the photon, also called inelasticity.

These variables can be expressed in terms of the scattered positron energy, E'_e, and angle, θ_e, both experimentally measurable. In the limit of $\theta_e \approx 0$, such as in the photoproduction process, the following approximations may be performed:

$$Q^2 = 2E_e E'_e(1 - \cos\theta_e) \approx E_e E'_e \theta_e^2, \tag{3.1}$$

$$y = 1 - \frac{E'_e}{2E_e}(1 + \cos\theta_e) \approx 1 - \frac{E'_e}{E_e}, \tag{3.2}$$

$$W \approx 2\sqrt{E_e E_p y}, \tag{3.3}$$

where E_e and E_p are the energies of the incident positron and proton, respectively.

3.3 Energy dependence calculation method

In e^+p collisions, the total photoproduction cross section, $\sigma_{\text{tot}}(\gamma p)$, can be related to the total differential ep cross section by the Weizsäcker-Williams formula [29]. The double-differential e^+p cross section can be written as

$$\begin{aligned}\frac{d^2\sigma^{e^+p}(y,Q^2)}{dydQ^2} = \frac{\alpha}{2\pi Q^2}\left[\frac{1+(1-y)^2}{y} - 2\frac{(1-y)}{y}\frac{Q^2_{min}}{Q^2}\right]\sigma_T^{\gamma p}(y,Q^2) \\ + \frac{\alpha}{2\pi Q^2}\left[\frac{2(1-y)}{y}\right]\sigma_L^{\gamma p}(y,Q^2),\end{aligned} \tag{3.4}$$

where $Q^2_{min} = m_e^2 \frac{y^2}{1-y}$ is the minimum value of Q^2 at a given y, $\sigma_T^{\gamma p}$ is the cross section for interactions between the proton and a photon with transverse polarization and $\sigma_L^{\gamma p}$ is the cross section for interactions with longitudinally polarized photons.

For photoproduction events, $Q^2 \to 0$ and the photon is almost real. Hence, $\sigma_L^{\gamma p} \to 0$ and $\sigma_T^{\gamma p} \to \sigma_{\text{tot}}(\gamma p)$.
The Q^2 dependence of $\sigma_T^{\gamma p}$ is smaller than 0.1% in the range of Q^2 of this measurement and therefore it has been ignored [3]. Integrating Eq. (3.4) over Q^2 gives the single e^+p differential cross section in terms of the γp total cross section:

$$\frac{d\sigma^{e^+p}(y)}{dy} = \frac{\alpha}{2\pi}\left[\frac{1+(1-y)^2}{y}\ln\frac{Q^2_{max}}{Q^2_{min}} - 2\frac{(1-y)}{y}\left(1-\frac{Q^2_{min}}{Q^2_{max}}\right)\right]\sigma^{\gamma p}_{\text{tot}}(y), \tag{3.5}$$

where Q^2_{max} is the highest measured Q^2 given by the acceptance of the 6mT. Integrating Eq. (3.5) over y gives the e^+p cross section

$$\sigma^{e^+p} = \int_{y_1}^{y_2} F_\gamma(y)\sigma^{\gamma p}_{\text{tot}}(y)\, dy, \tag{3.6}$$

where $F_\gamma(y)$ is the flux of photons emitted by the positron and y_1 and y_2 are derived from the minimum and maximum detected positron energies, respectively.
Assuming $\sigma_{\text{tot}}(\gamma p) \sim W^\delta$ (see chapter 1), the ratio R can be expressed as

$$\begin{aligned} R = {} & \frac{\sigma^{e^+p}_{\text{HER}} \cdot \sigma^{e^+p}_{\text{HER}}}{\sigma^{e^+p}_{\text{MER}} \cdot \sigma^{e^+p}_{\text{LER}}} = \\ = {} & \frac{\int_{y^{\text{HER}}_{\text{min}}}^{y^{\text{HER}}_{\text{max}}} F_{\text{HER}}(y)(W_{\text{HER}}(y))^\delta\, dy \int_{y^{\text{HER}}_{\text{min}}}^{y^{\text{HER}}_{\text{max}}} F_{\text{HER}}(y)(W_{\text{HER}}(y))^\delta\, dy}{\int_{y^{\text{MER}}_{\text{min}}}^{y^{\text{MER}}_{\text{max}}} F_{\text{MER}}(y)(W_{\text{MER}}(y))^\delta\, dy \int_{y^{\text{LER}}_{\text{min}}}^{y^{\text{LER}}_{\text{max}}} F_{\text{LER}}(y)(W_{\text{LER}}(y))^\delta\, dy}. \end{aligned} \tag{3.7}$$

$W(y)$ is given by Eq. (3.3) and the ranges for y are determined for each period separately (see Sect. 3.4.2).

Determining R experimentally would provide a measurement of δ, using Eq. (3.7). Section 3.4 describes the process of measuring R.

3.4 Energy dependence measurement

Measuring the ratio R requires three measurements of σ^{e^+p}, one for each run, HER, MER and LER. The cross section, $\sigma^{e^+p}_{\text{HER}}$, is measured experimentally by

$$\sigma_{\mathrm{HER}}^{e^+p} = \frac{N_{\mathrm{HER}}}{A_{\mathrm{HER}} \cdot \mathcal{L}_{\mathrm{HER}}}. \tag{3.8}$$

The luminosities are measured with the LUMI system in each run and the acceptances are calculated using a Monte-Carlo simulation (see Sect. 4.4). The heart of this analysis is to count the number of events in each run and to reject background events.
The three measurements are then combined to give R,

$$R = \frac{N_{\mathrm{HER}}^2}{N_{\mathrm{MER}} N_{\mathrm{LER}}} \cdot \frac{A_{\mathrm{MER}} A_{\mathrm{LER}}}{A_{\mathrm{HER}}^2} \cdot \frac{\mathcal{L}_{\mathrm{MER}} \mathcal{L}_{\mathrm{LER}}}{\mathcal{L}_{\mathrm{HER}}^2}. \tag{3.9}$$

In the experimental apparatus used, a photoproduction process is expected to have a low angle scattered positron hitting the 6mT and some hadronic activity in the main calorimeter. According to these characteristics, a dedicated trigger was set in order to count photoproduction events.

3.4.1 Trigger requirements

A dedicated trigger was developed to collect photoproduction events [21]. Two conditions were required: a positron candidate in the 6mT and a hadronic final-state X in the main ZEUS detector. The 6mT trigger required energy above the threshold in one of the cells in rows one or two (see Fig. 2.2). The following FLT slots required a hit in the 6mT and the subsequent conditions:

- slot 30: the energy in PCAL, $E_{\mathrm{PCAL}} > 14$ GeV (this slot was pre-scaled by 4096).
- slot 51: a good tracking flag, G_{trk}, and $E_{\mathrm{PCAL}} < 14$ GeV.
- slot 52: the energy in the electromagnetic section of RCAL, excluding the inner ring (the 8 innermost towers surrounding the beam-pipe), $RCAL_{emc} \geq 464$ MeV and $E_{\mathrm{PCAL}} < 14$ GeV.
- slot 53: the energy in the electromagnetic section of RCAL, $RCAL_{emcth} \geq 1250$ MeV and $E_{\mathrm{PCAL}} < 14$ GeV.

- slot 59: $RCAL_{emc} \geq 464$ MeV or $RCAL_{emcth} \geq 1250$ MeV and $E_{\mathrm{PCAL}} <$ 14 GeV (logic 'or' of slot 52 and slot 53).

A logic 'or' of all the above slots was required in the dedicated trigger.

An additional FLT requirement was applied in the HER, a veto on the ratio of vertex tracks to the total number of tracks. This veto was not implemented in the MER and LER. Therefore, in order to ensure equal trigger conditions in the HER, MER and LER, a slightly tighter veto was applied off-line in all the runs.

3.4.2 6mT

The 6mT performed three roles in this measurement: tagging positrons emanating from photoproduction processes, measuring the energy range of the positrons and determining the flux of photons emitted by the positrons.

Detecting positrons

Positrons scattered at very low angles ($Q^2 \approx 0$) with energies between 4-8 GeV were bent horizontally and focused vertically by the magnetic field on their way to be tagged by the 6mT. The Lorentz force states that the curvature of the positron depends on its momentum. As a result, a dependence between the energy of the positron and its position is expected.
Using a control sample of BH positrons, scattered at $Q^2 = 0$, it is possible to derive a parameterization of the dependence of energy on the position and define a band of accepted energies and positions in the $E - x$ plane and the $x - y$ plane. This is used to reject noise and other background events.

Energy range measurement

The energy window for positrons hitting the 6mT was fixed by the width of the tagger. Moreover, the fiducial cut applied on 6mT hits (see Sect. 4.3.1) limited the window even further. The energy of scattered positrons in the 6mT was measured directly. However, it has been shown in a previous study that the energy resolution using the x position and the $E(x)$ parameterization mentioned above is better than the direct measurement [21]. Thus, a measurement of the range of x positions accepted by the fiducial cut, together with the $E(x)$ parameterization, was used to determine the energy window. Using the relation $y \approx 1 - \frac{E'_e}{E_e}$, the energy window, for each run, was determined to be

- HER: $y_{\rm min} = 0.7397$, $y_{\rm max} = 0.8623$;
- MER: $y_{\rm min} = 0.7373$, $y_{\rm max} = 0.8575$;
- LER: $y_{\rm min} = 0.7449$, $y_{\rm max} = 0.8601$.

Photon flux measurement

The process of extracting $\sigma_{\rm tot}(\gamma p)$ from σ^{e^+p} required a calculation of the flux of photons emitted by the positrons. However, using Eq. (3.5) for this calculation would have ignored the dependence of the acceptance of the 6mT ($A_{\rm 6mT}(y, Q^2)$) on the kinematic y and Q^2. Therefore, it was necessary to measure $A_{\rm 6mT}(y, Q^2)$, convoluted with the flux, from the data.
A further advantage of a direct measurement of the 6mT flux is that it accounts for several effects which would otherwise require corrections to the data:

- 6mT trigger efficiency;
- 6mT selection acceptance - the cuts depicted in Sect. 4.3.1 can be made arbitrarily tight to reduce background;
- 6mT inhomogeneities, e.g. weak fibers or miscalibration;
- 6mT noisy cells;
- 6mT corrupt data (see Sect. 4.1.1).

A data set selected without the requirement of a positron candidate in the 6mT may be used to measure the photon flux of positrons hitting the tagger [30].
An inclusive trigger, requiring $E - P_z > 30$ GeV, was used to collect events. An example of the kinematic region covered by this trigger is shown by the vertical dashed line in Fig. 3.1. The data selected have a fraction $r_{\rm 6mT}$ of events with hits in the 6mT with respect to events collected by the inclusive trigger. The acceptance of the 6mT is sketched by the shaded ellipse in

Fig. 3.1. Using the Monte-Carlo simulation of that inclusive selection of events, some fraction r_{MC} of these events is selected within a given test region of (y, Q^2), shown by the box in Fig. 3.1. The flux corresponding to this region, F_{test}, may be easily evaluated numerically using Eq. (3.5). The 6mT flux, F_{6mT}, can then be related to F_{test} by:

$$F_{\mathrm{6mT}} = \frac{N^{\mathrm{6mT}}_{\mathrm{data}}}{N^{\mathrm{all}}_{\mathrm{data}}} \cdot \frac{N^{\mathrm{all}}_{\mathrm{MC}}}{N^{\mathrm{test}}_{\mathrm{MC}}} \cdot F_{\mathrm{test}} = \frac{r_{\mathrm{6mT}}}{r_{\mathrm{MC}}} \cdot F_{\mathrm{test}}, \tag{3.10}$$

provided that the kinematic range of the inclusive trigger in the Monte-Carlo simulation and the data agree.

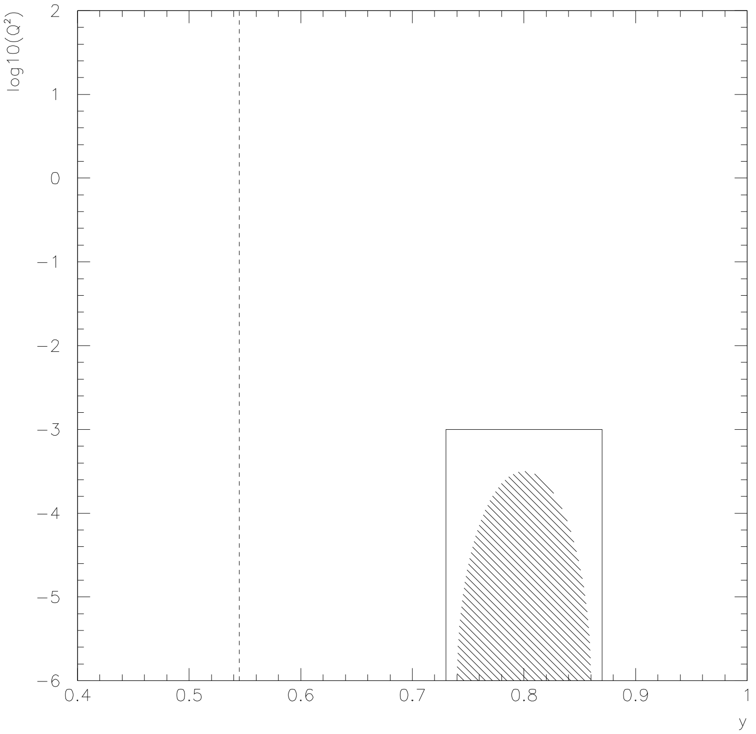

Figure 3.1: The (y, Q^2) plane. The approximate threshold of the $E - P_z$ trigger is shown by the vertical dashed line. The test region for numerical evaluation of the test flux is shown by the box; the acceptance of the 6mT is sketched by the shaded ellipse.

3.5 Background

Many non-photoproduction events were expected and found in the data collected by the triggers. These events are referred to as background events. The energy deposited in RCAL, E_{RCAL}, was used in the trigger to collect photoproduction events. Hence, E_{RCAL} distribution in data and Monte-Carlo will be used in subsequent comparisons while attempting to reject background events. Figure 3.2 shows such a comparison and clearly demonstrates a discrepancy between the distribution obtained in the triggered data and expected in the Monte-Carlo.
Subsequently there is a description of background events and their origin.

3.5.1 Bethe-Heitler process

A big source of background expected is Bethe-Heitler events overlaid with any physics event or noise in the main detector. In such events, a high energy photon is expected to hit the PCAL accompanied by a positron in the 6mT and the energy of the two must add up to the energy of the beam. The window for BH photons hitting the PCAL is therefore limited by the window of energies for positrons hitting the 6mT mentioned in Sect. 3.4.2. In order to avoid collecting BH events, activity in the CTD/RCAL was required in the trigger and a veto was set to reject all events with energies higher than 14 GeV in the PCAL. Alas, the PCAL acceptance is not 100% and it is probable that some events were triggered by a BH positron in the 6mT and some other process in the main detector. This could also happen with photons lost in the exit window and converted in the spectrometer. A method to count and statistically subtract such overlapping events is described in Sect. 4.6.1.

3.5.2 *e*-gas events

Beam-gas events were another source of background. A positron interacting or scattering off residual gas in the beam-pipe deposits energy in RCAL; if this happens in coincidence with a hit in the 6mT the event will be accepted by the trigger. A technique to identify and discard these events is outlined in Sect. 4.3.3. *e*-pilot bunches provided a mechanism to estimate the number of beam-gas events not identified and to subtract them statistically (see Sects. 4.6.2).

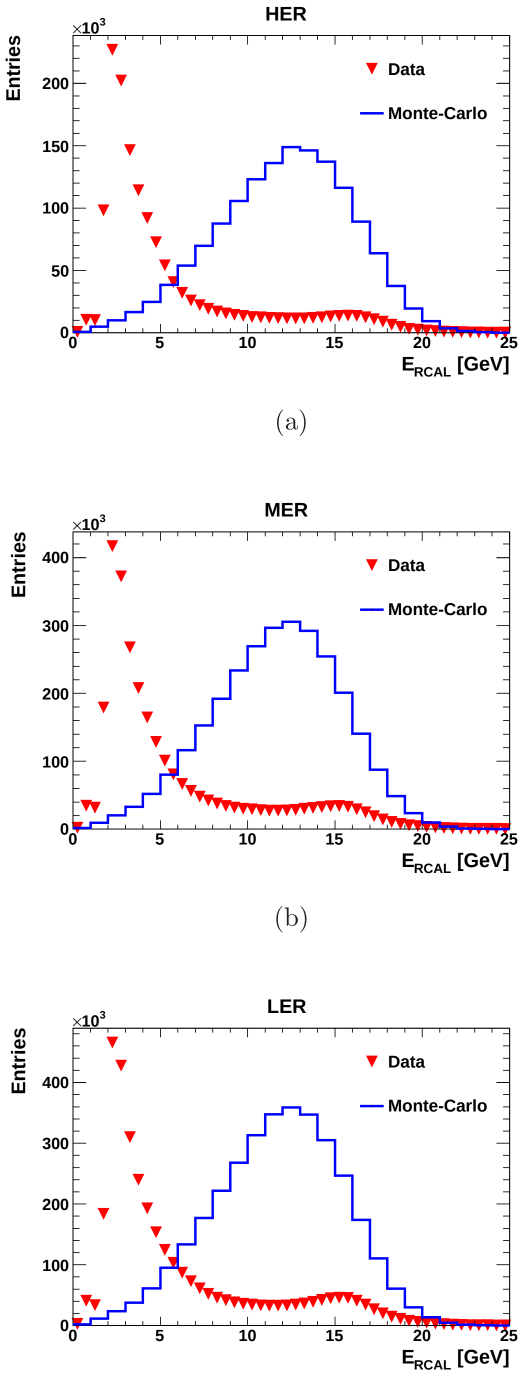

(a)

(b)

(c)

Figure 3.2: Distribution of energy deposited in the RCAL, E_{RCAL}, obtained in the triggered data (triangles) and the corresponding distribution expected in the Monte-Carlo (histograms) for (a) HER (b) MER and (c) LER.

3.5.3 Off-momentum positrons

A further source of background were positrons in the beam with $p_T \neq 0$. These positrons were bent by the magnetic field of the focusing HERA magnets placed before the IP and hit the RCAL tower left of the beam-pipe or the 6mT. Such positrons are referred to as off-momentum positrons. A description as to how off-momentum positrons were recognized and rejected is illustrated in Sects. 4.3.1 and 4.3.3.

Chapter 4

Data Analysis

The data samples collected with the dedicated trigger configuration consisted of 4,061,359 events in HER, 10,430,872 events in MER and 12,814,242 events in LER. These correspond to a luminosity of 566 nb^{-1}, 948 nb^{-1} and 912 nb^{-1} respectively.

4.1 Energy Reconstruction in the 6mT

A positron hitting the 6mT produces an electromagnetic shower and deposits most of its energy within several R_{M} of the center of the shower. Since R_{M} is of the order of the size of one cell, most of the energy is deposited in a few cells around the shower center. The energy deposited in a volume V in and around the cell with the highest energy, the *hottest cell*, was taken as the energy E of the shower.

In a previous study [20] it was found that only about 1 to 5% of the total energy is deposited in the outer columns of a 5×5 volume around the hottest cell (50 to 200 MeV). This signal is comparable to the noise level and therefore, to reduce noise effects, the volume used for energy reconstruction was set to nine cells, a 3×3 matrix with the hottest cell in the center (see Fig. 4.1). In addition, to obtain an accurate reconstruction of energy, only events where the shower was contained in the tagger were taken (i.e. the hottest cell was not in the outer cells of the 6mT).

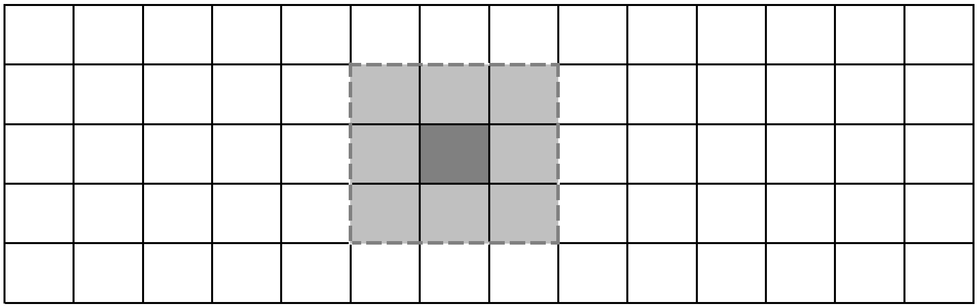

Figure 4.1: Schematic representation of the volume used for energy reconstruction in the 6mT. The darkest cell corresponds to the cell with highest energy deposit. The shaded area represents the cells included in the energy determination.

4.1.1 Corrupted events

Events having ADC counts corresponding to non-physical energy values were found in the data taken with the 6mT. The data acquisition system of the 6mT converted the analogue signal of the photomultipliers to unsigned 12-bit numbers with ADC's, transferred the signal to five readout boards, one for each row, and added four empty bits to each ADC count, leading to 16-bit numbers stored for further processing. The corruption of the ADC counts manifested itself in having ADC counts which exceeded the range of unsigned 12-bit numbers (0 to 4095) in one or more of the 70 channels of the 6mT. This problem occurred in all 70 channels randomly. In order to avoid using non-physical energies in the energy reconstruction and selection process (see Sect. 4.3.1), events with ADC counts in the 5×5 matrix around the hottest cell which were not in the range 0 to 4095 were rejected.

4.1.2 Noise correction

The 6mT had two noisy cells. Figure 4.2 shows the energy of the hottest cell in row 3 of the 6mT. The excess of events seen in cells 10 and 12 of row 3 and the energy of these cells leads to the conclusion that they are noisy. The energy does not lie inside the band populated by events in which scattered positrons with transverse momentum $p_{\mathrm{T}} \approx 0$ GeV are expected.
Studying events triggered by noisy cells demonstrated that the signal is con-

fined to a single cell and does not show a topology compatible with an electromagnetic shower. Therefore, the noise is believed to be caused by electronics [20]. Figure 4.3a shows the energy distribution in a 3×3 matrix of events triggered by a noisy cell; Fig. 4.3b shows the same matrix for events triggered by a normal cell. One can see that in electromagnetic showers, 45% of the energy is confined to the hottest cell whereas in events triggered by noise, 70% of the energy lies in the hottest cell.

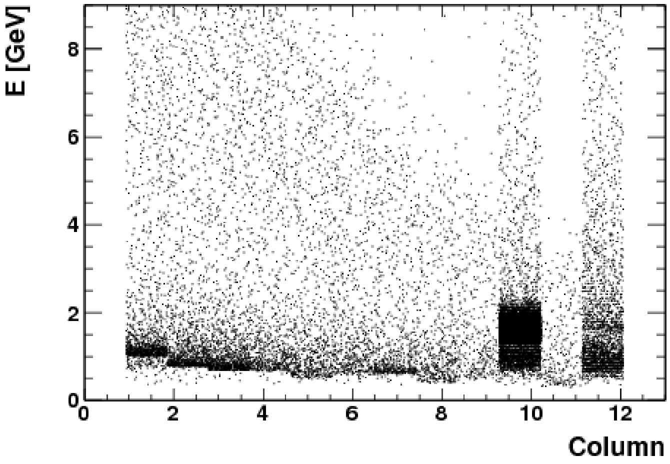

Figure 4.2: Reconstructed energy, E, as a function of the column number associated with the hottest cell located in the third row of the 6mT.

Trigger requirements in the 6mT were set such that events with the hottest cell in the 3rd row were globally rejected. As a result, events could not be triggered by the noisy cells. Events where the hottest cell was found to be one of the noisy cells were rejected in the analysis. However, when the 3×3 matrix included one (or both) noisy cells, the energy measured by them was not to be trusted and needed to be re-evaluated differently. Using the energies measured in the other 8 cells in the 3×3 matrix, a neural network (NN) was used to evaluate the energy in the noisy cell.

NN training

A clean data sample was obtained for the process of training the neural network by using the cuts described in Sects. 4.3.2, 4.3.3 and requiring the

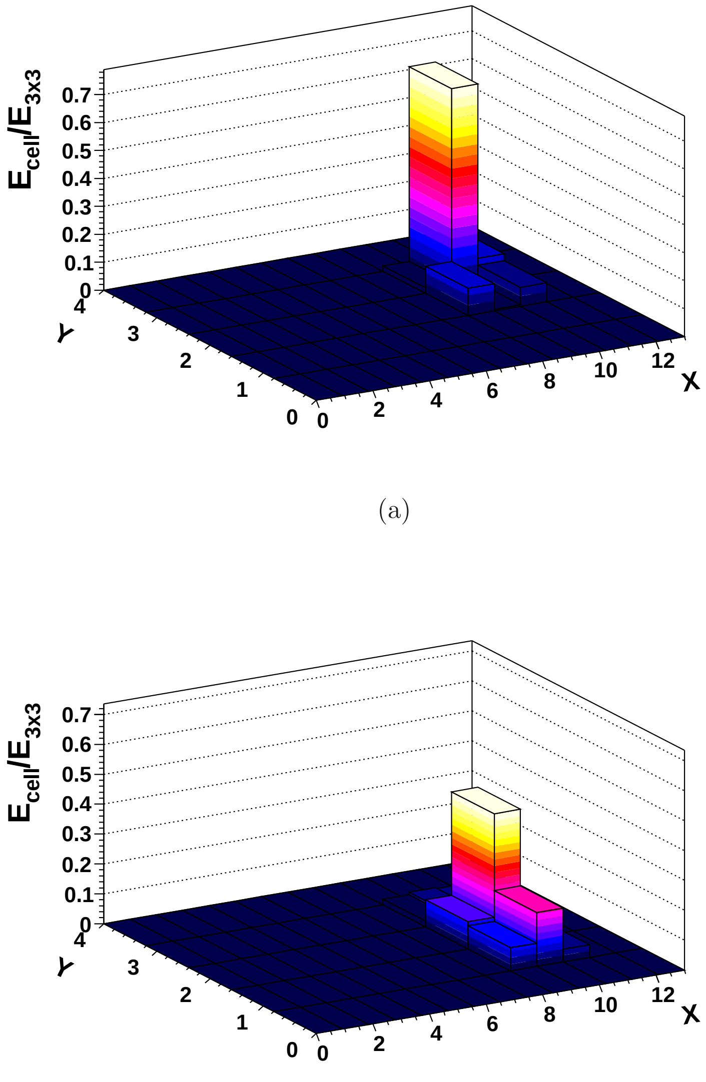

(a)

(b)

Figure 4.3: Distribution of energy in showers of events triggered by (a) cell 10 of row 3 (noisy cell) and (b) cell 10 of row 2 (normal cell).

energy in the 6mT to be between 2 and 9.5 GeV. The data fed into the neural network consisted of x and y positions of the hottest cell and a matrix of 9 energies. One of the energies in the matrix was set to zero to represent the energy that should be completed. The cell energy before masking was given as a true value. Events in which the matrix included a noisy cell were not used. All values were normalized to 1, but it was found that a better result was obtained using a logarithm of the energy in each cell and not a simple normalization, presumably due to the better separation the log provides.

In each event used for the training, the 3×3 matrix was taken and one cell in the matrix was masked. This process was repeated 9 times, each time masking a different cell in the matrix, resulting in 9 entries to the training data set from each positron shower. Each entry represents a different position of the noisy cell in the matrix.

Outcome

The neural network configuration yielding the best result consisted of two hidden layers with 25 neurons in the first layer and 5 neurons in the second. Figure 4.4a shows the difference between the energy completed with the neural network (E_{NN}) and the energy in the cell before masking (E_{true}), for all cell positions in the matrix. The tail at negative values points to the fact that in about 15% of the cases the neural network under-estimates the energy in the cell, but otherwise we have a gaussian centered at zero. A fit to the gaussian part of the distribution gives a standard deviation from the true energy in the cell of about 280 MeV.

Aftermath of noise correction

To check the effect of completing the energy of a masked cell on the position reconstruction, the same process as described above was repeated with a Monte-Carlo simulation. Figure 4.4b shows the neural network result in the simulation. It can be seen that the tail at negative values there was in the data is still present in the simulation, only it is smaller in this case (about 11%). A fit to the gaussian part yields a standard deviation from the true energy of about 260 MeV. This is a cross-check that the electromagnetic shower in the simulation and in reality develops in the same way.

Two energy matrices were fed into the position reconstruction neural network described in Sect. 4.2, one with the original energies measured in the cells and one where one of the energies was masked and then re-evaluated using

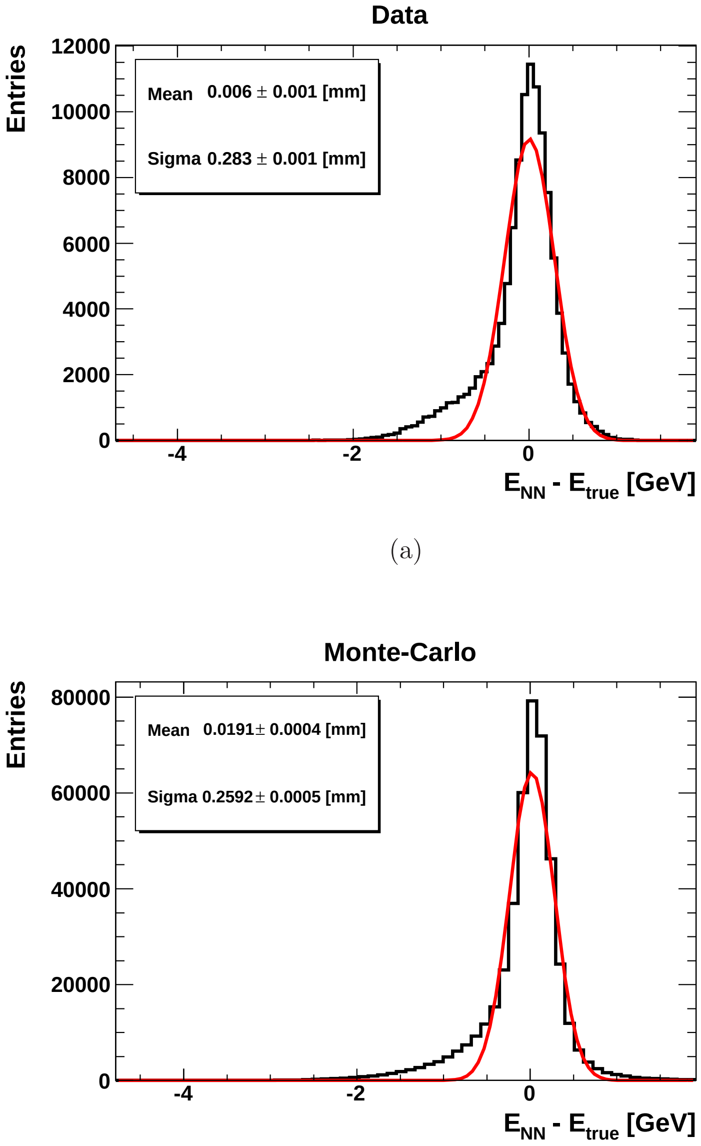

(a)

(b)

Figure 4.4: The difference between the re-evaluated cell energy (E_{NN}) and the original cell energy (E_{true}) for all cell positions in the 3×3 matrix in (a) data and (b) Monte-Carlo simulation. The results of a gaussian fit are presented in the figure.

the neural network. Figure 4.5 shows the difference between the x position, reconstructed from a re-evaluated matrix ($x_{\rm rec}^{\rm com}$), and the true x position ($x_{\rm true}$) from the simulation. This was compared to the difference between the x position reconstructed from the original energies ($x_{\rm rec}$) and the true value (see Fig. 4.6b). Comparing Fig. 4.5 with Fig. 4.6b, it is possible to see that the completion process introduced a negligible bias (≈ 0.04 mm) and a minimal loss of resolution (≈ 0.01 mm).

All the energies used in this analysis were corrected with the neural network described above, where needed.

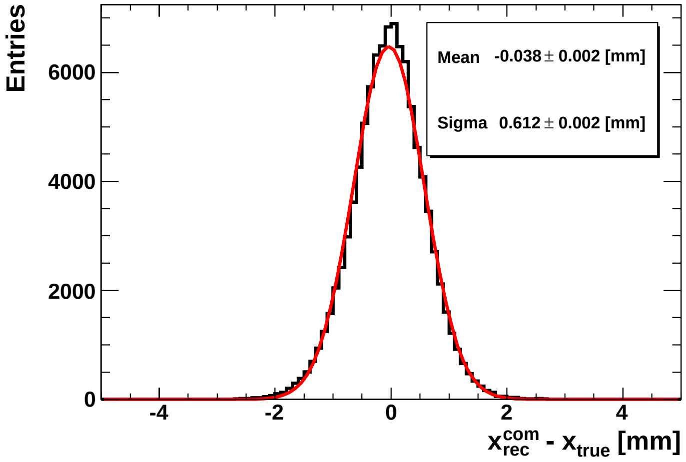

Figure 4.5: The difference between the x position, reconstructed from a re-evaluated energy matrix ($x_{\rm rec}^{\rm com}$), and the true x position from the simulation ($x_{\rm true}$). The results of a gaussian fit are presented in the figure.

4.2 Position reconstruction in the 6mT

The original reconstructed x position of the positron in the 6mT, shown in Fig. 4.6a, had a bias of 1.78 mm and a resolution of 0.67 mm. Using the Monte-Carlo simulation and a neural network, an attempt was made to eliminate the bias and to improve the resolution.

For the training process, the neural network was given a matrix of 9 energies and 3 column positions, the column of the hottest cell and the columns

on both sides of it. The real x position of the positron, taken from the simulation, was given as the true value. The column positions and the true value were normalized to 1.
The optimal configuration of the neural network was with one hidden layer of 43 neurons. Figure 4.6b shows the difference between the reconstructed x position (x_{rec}) and the true value. As can be seen, the bias was completely eliminated and the resolution improved to 0.59 mm.

The same process was repeated for the y position of the positron. The data used for training was identical to the case of the x position, apart from replacing rows by columns and the real y position given as the true value. In this case, the optimal neural network configuration was with one hidden layer of 23 neurons.
A comparison between the original y position reconstruction and the neural network result (Figs. 4.7a and 4.7b) demonstrates a reduction of the bias from 0.16 mm to 0.09 mm, while the resolution changed only slightly (from 0.46 mm to 0.45 mm).

4.3 Selection cuts

The background discussed in Sect. 3.5 is suppressed using the cuts described below.

4.3.1 6mT

Fiducial

In Sect. 4.1, it was mentioned that events were accepted only if the electromagnetic shower created by the positron was contained in the 6mT. In addition, the trigger in the 6mT fired only for hits in rows 1 and 2. Events with hits not in these rows were rejected. Hence, the hottest cell was constrained as follows:

$$0 < \text{Column}~\# < 13$$
$$0 < \text{Row}~\# < 3$$

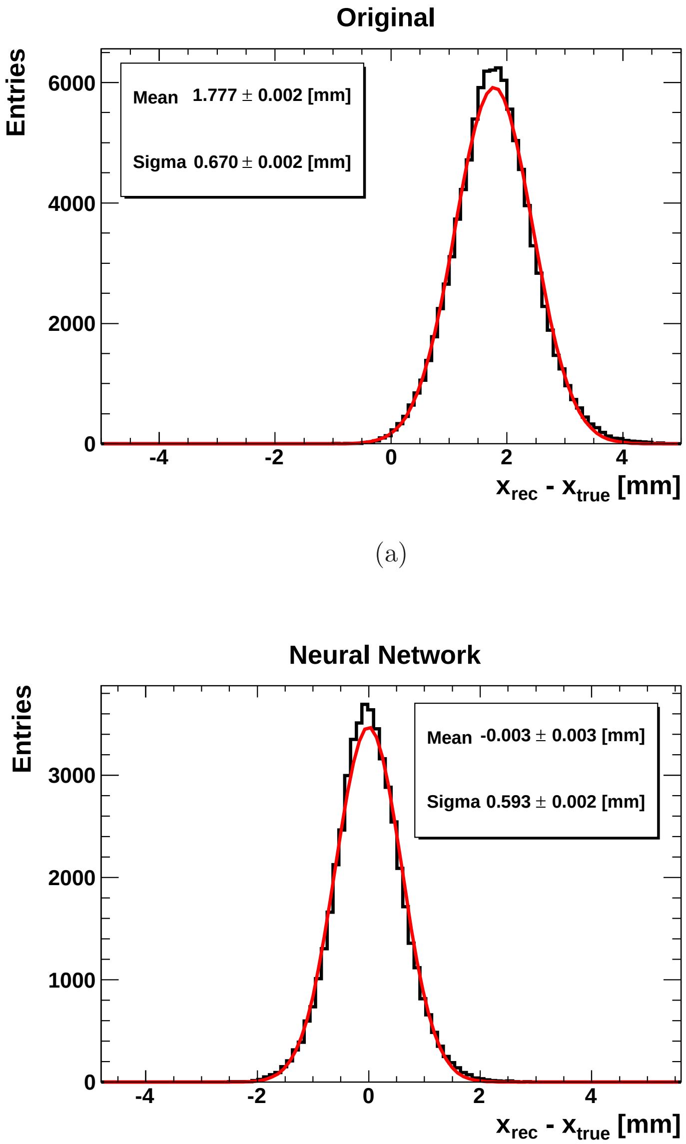

(a)

(b)

Figure 4.6: The difference between the reconstructed x position (x_{rec}) and the true x position (x_{true}) in (a) original 6mT group reconstruction and (b) neural network reconstruction. The results of a gaussian fit are presented in the figure.

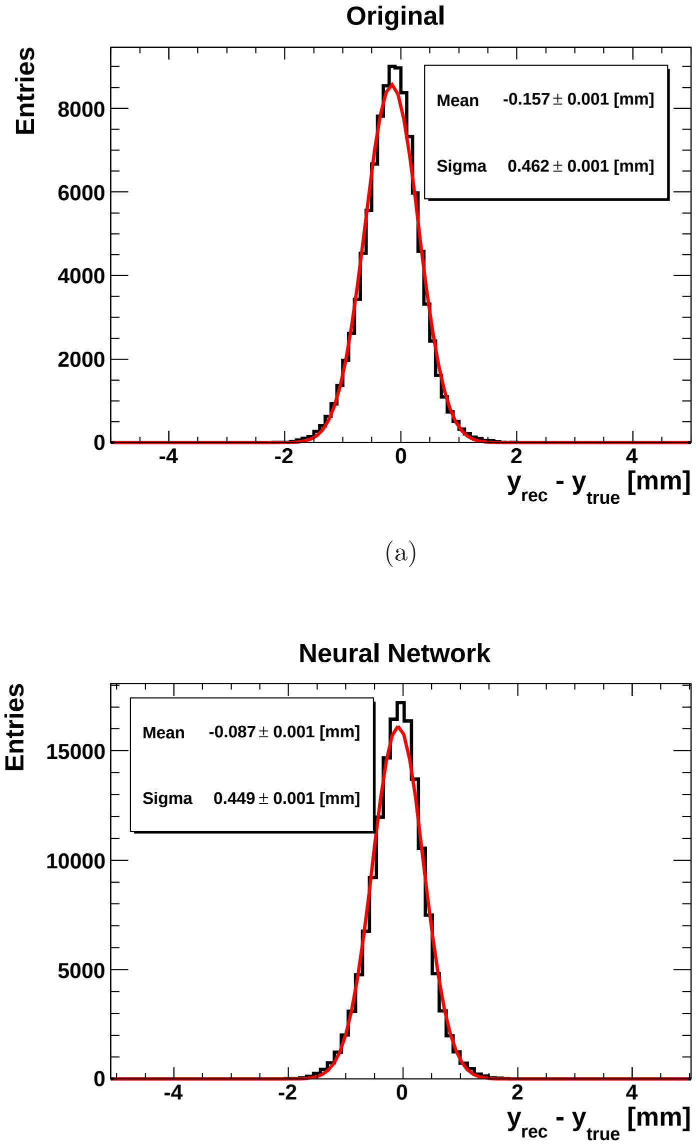

(a)

(b)

Figure 4.7: The difference between the reconstructed y position (y_{rec}) and the true y position (y_{true}) in (a) original 6mT group reconstruction and (b) neural network reconstruction. The results of a gaussian fit are presented in the figure.

Splash

In about 1% of the events [31], the positron began its electromagnetic shower before reaching the 6mT and deposited energy in an area bigger than the 3×3 matrix used for energy reconstruction. In these cases, neither the position nor the energy of the positron could have been reconstructed. In order to avoid these "splash" events, the ratio $\mathrm{E}_{3\times3}/\mathrm{E}_{5\times5}$ was calculated for each event and was required to be above 0.65. This requirement is consistent with a previous study [20] which states that about 1 to 5% of the total energy is deposited in the outer columns of the 5×5 matrix.

$E(x)$ band

Positrons scattered at the interaction point with $Q^2 \approx 0$ GeV^2 are expected to have a correlation between their energy and x position. Using this correlation from BH events, a cut can be extracted to reject noise, beam-gas events and off-momentum positrons hitting the 6mT. A clean data sample of BH events was acquired by requiring a coincidence between a positron in the 6mT and a photon in the spectrometer [32].

It can be seen in Fig. 4.8 that most of the events lie within the expected band for positrons scattered with $Q^2 \approx 0$ GeV^2. The curve represents the mean reconstructed energy as a function of x position, $E(x)$. It was parameterized separately for HER, MER and LER together with $\sigma_E(x)$, the standard deviation of the energy as a function of x.
Using these parameterizations, a cut was made to reject events outside the band defined by

$$E(x) - 2.5\sigma_E(x) < E < E(x) + 2.5\sigma_E(x).$$

Figure 4.9 shows the E versus x distribution for LER data. The curves correspond to the BH parameterization and the above defined band cut. The HER and MER data show a similar behaviour.

$y(x)$ band

Due to the focusing magnets in the y direction, positrons hitting the 6mT were highly collimated vertically. In addition, because the focusing depends on the energy of the positron and there is a correlation between energy and x position, we also expect a correlation between y and x. Repeating the

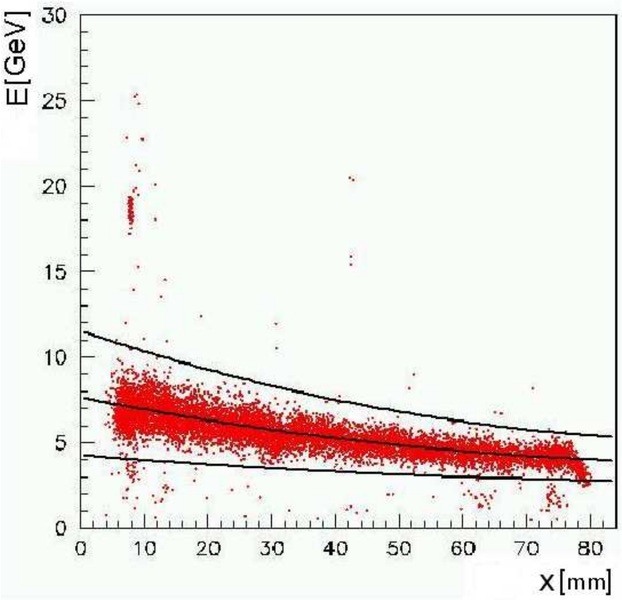

Figure 4.8: Energy in the 6mT (E) as a function of x position obtained from the BH data sample.

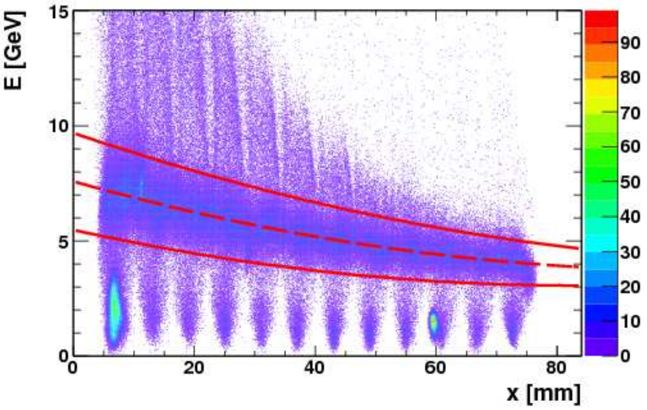

Figure 4.9: The energy measured in the 6mT (E) as a function of the reconstructed x position, for the LER data. The center curve shows the parameterization based on the BH sample. The upper and lower lines are the $2.5\sigma_E(x)$ limits, where $\sigma_E(x)$ is the standard deviation of the energy as a function of x.

process described above to extract a clean data sample of BH events, a parameterization of $y(x)$, together with $\sigma_y(x)$, was extracted for HER, MER and LER separately. Events were accepted only in the region where

$$y(x) - 2.5\sigma_y(x) < y < y(x) + 2.5\sigma_y(x).$$

Figure 4.10 shows the y versus x distribution for the HER data with curves representing the band defined above. The MER and LER data show a similar behaviour.

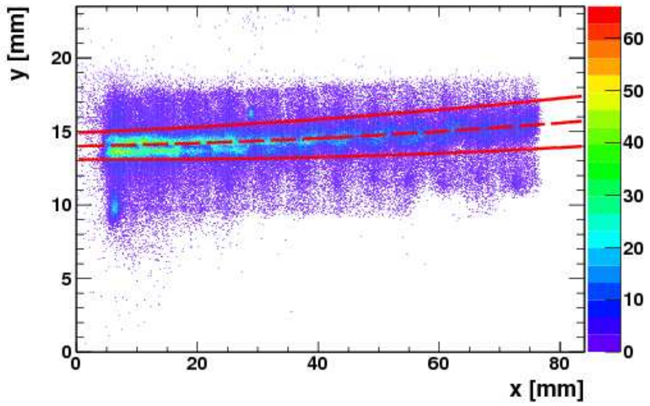

Figure 4.10: Reconstructed y position as a function of x position. The center curve shows the parameterization done with the BH sample. The upper and lower lines are the $2.5\sigma_y(x)$ limits, where $\sigma_y(x)$ is the standard deviation of y as a function of x.

4.3.2 Trigger

A closer look at the data revealed events which should not have passed the trigger requirements described in Sect. 3.4.1, specifically slots 52, 53 and 59. It was discovered [33] that in these events the trigger fired for false reasons and therefore, they needed to be eliminated with an off-line trigger. These false trigger events occurred randomly during the collection of data while for other events the trigger worked correctly. Hence, a method to apply a consistent trigger to all events was needed.

For this purpose, all events in this analysis were subjected to a simulation of the entire process of the original trigger. This guaranteed a consistent trigger for all events while rejecting noise and background. Figure 4.11 compares the energy in RCAL in the MER data and in the Monte-Carlo before and after the application of the trigger simulation. Before applying the trigger simulation, a large amount of events is found at low RCAL energy in the data and a big discrepancy between the data and the Monte-Carlo is seen. The same is true for the HER and LER data (not shown).

4.3.3 F_{max}

Many events that passed slot 53 of the trigger requirements ($\geq$ 1250 MeV) were composed of hits confined to one RCAL tower left or right of the beam-pipe. These events were identified as off-momentum positrons or positrons coming from beam-gas interaction in the beam-pipe and hitting the RCAL. This appeared to be one of the biggest sources of background and it had to be eliminated.

For events in which the cell with maximum energy deposit in RCAL was to the left or right of the beam-pipe, the following variable was defined:

$$F_{\mathrm{max}} = \frac{E_{\mathrm{l,r}}}{E_{\mathrm{RCAL}}},$$

where $E_{\mathrm{l,r}}$ is the energy of the tower to the left or right of the beam-pipe and E_{RCAL} is the total energy in RCAL. Figure 4.12 shows the correlation between F_{max} and RCAL energy for the LER data and Monte-Carlo. It can be seen that, in the case of the Monte-Carlo, most of the events have energies between 5 and 20 GeV and F_{max} values between 0.1 and 0.5. In the data, on the other hand, one can see a large cluster around $F_{\mathrm{max}} = 1$ belonging to off-momentum positrons hitting the RCAL. Furthermore, a cluster at smaller values of F_{max} and lower RCAL energies is also found in the data. These events originate from positrons interacting with beam-gas and, together with other debris, hitting the RCAL. In order to confirm these hypotheses, the same distribution was plotted for e-pilot bunches (see Fig. 4.13) in the LER data. For these bunches, most of the events did lie in the clusters described above. The HER and MER data show a similar behaviour.

A cut on F_{max} and E_{RCAL}, as seen in Fig. 4.12, was made to reject such events. The Monte-Carlo distribution shows that by introducing this cut the same percentage (9%) of events was lost in HER, MER and LER. This loss cancels out when taking the ratio of numbers of events in the final calculation.

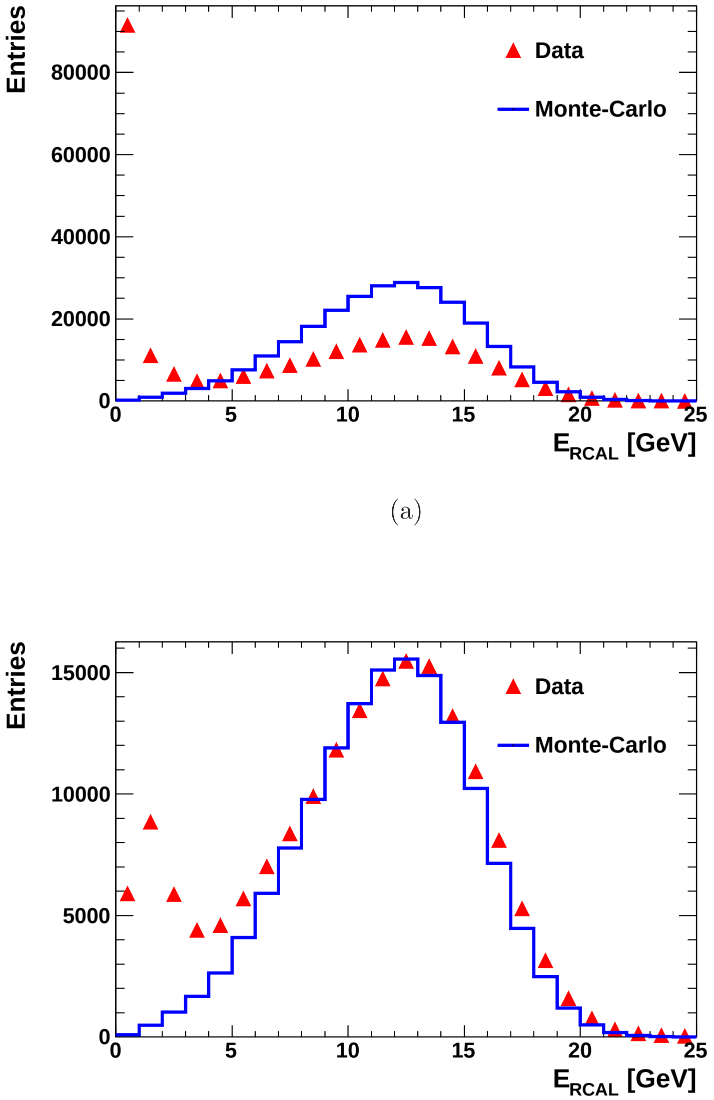

(a)

(b)

Figure 4.11: Distribution of energy deposited in the RCAL, E_{RCAL}, obtained in the MER data (triangles) and the corresponding distribution expected in the Monte-Carlo (histograms), (a) before applying the trigger simulation and (b) after applying the trigger simulation.

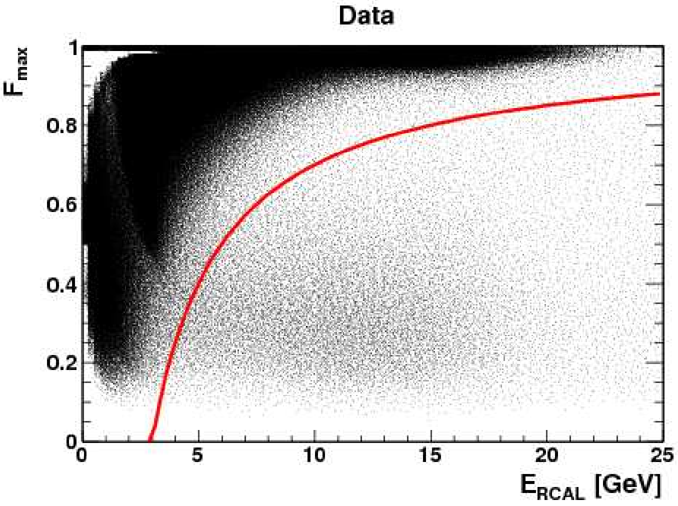

(a)

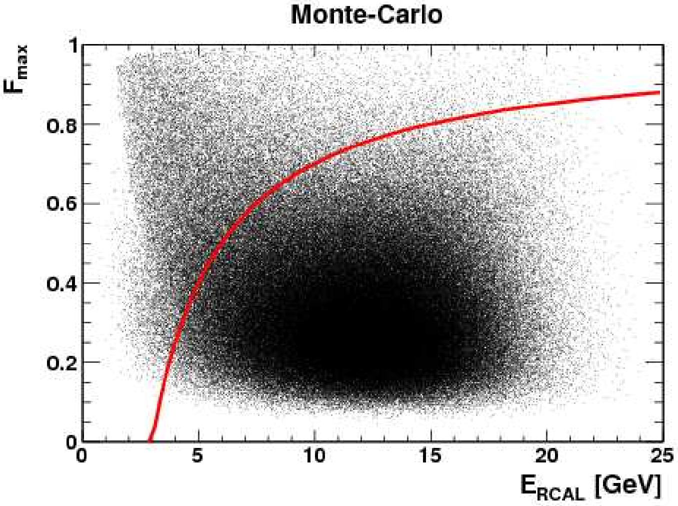

(b)

Figure 4.12: The $F_{\max}$ variable as a function of the energy deposited in the RCAL, E_{RCAL}, in (a) data and (b) Monte-Carlo. All events above the curve were rejected.

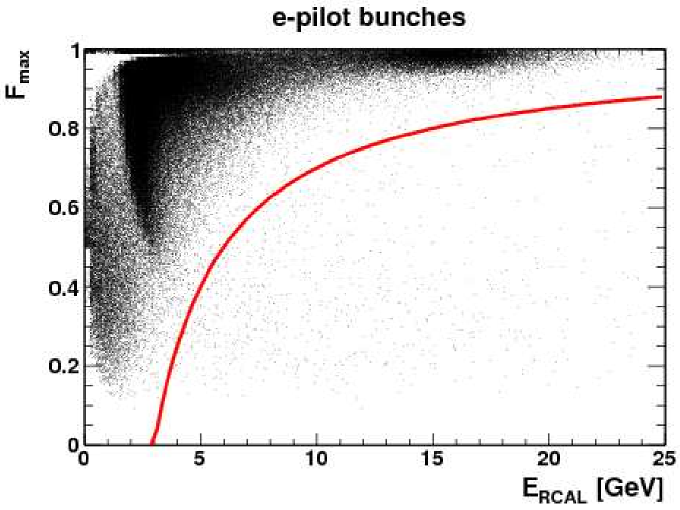

Figure 4.13: The F_{max} variable as a function of the energy deposited in the RCAL, E_{RCAL}, for e-pilot bunches.

4.3.4 Summary of selection cuts

A comparison between data and Monte-Carlo distributions of E_{RCAL}, after all the above mentioned cuts, is shown in Fig. 4.14 for HER, MER and LER. The peak at low RCAL energies seen in the data does not appear in the expected distribution. However, a statistical subtraction of background has not been performed yet.

4.4 Acceptance

The difference in center-of-mass energies between HER, MER and LER was obtained by changing the energy of the proton while keeping the positron energy constant. Hence, the trigger acceptance for photoproduction events was expected to remain the same in all three periods.

The acceptance of the ZEUS detector is composed of two independent acceptances: the acceptance of the main detector and the acceptance of the 6mT. The acceptance of the main detector is calculated using Monte-Carlo simulation. Simulated photoproduction processes were generated and passed through a simulation of the ZEUS detector. A simulation of the trigger de-

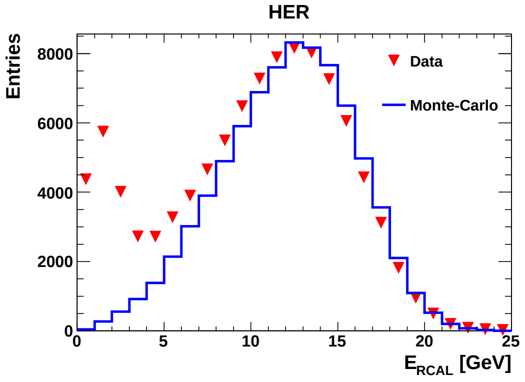

(a)

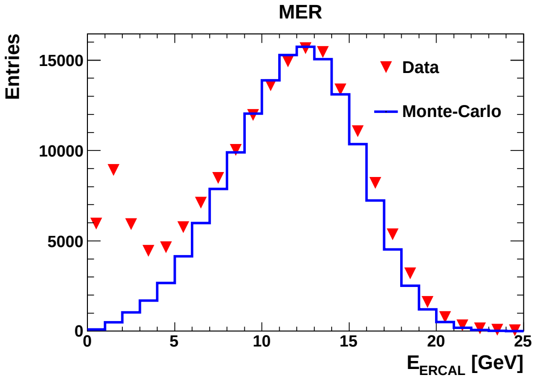

(b)

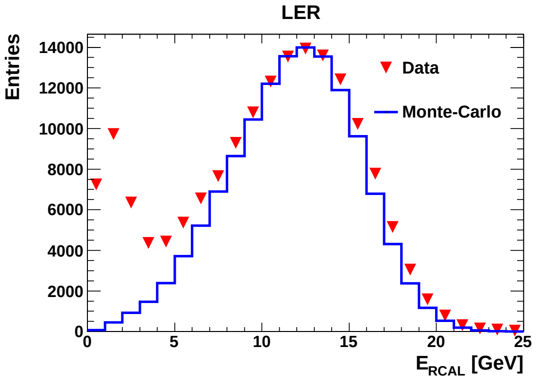

(c)

Figure 4.14: Distribution of energy deposited in the RCAL, E_{RCAL}, obtained in the data after all selection cuts (triangles) and the corresponding distribution expected in the Monte-Carlo (histograms) in (a) HER, (b) MER and (c) LER.

picted in Sect. 3.4.1 was implemented to collect events in the same way as for real data. Finally, the cuts relative to the main detector, namely Sects. 4.3.2 and 4.3.3, were applied and the acceptance was calculated according to

$$A = \frac{N_{\mathrm{rec}}}{N_{\mathrm{gen}}}, \tag{4.1}$$

where N_{rec} and N_{gen} are the number of reconstructed and generated events, respectively.

The same process cannot be performed for the 6mT due to changes in beam conditions and magnet settings between periods. Therefore, in order to isolate the acceptance of the main detector from that of the 6mT, only events generated within the energy window of the 6mT were taken.

In addition, it has been found that the sub-process mixture in the simulation does not describe the data optimally [27]. Thus, weights were applied to the fractions of the different sub-processes to ensure better agreement with the data.
The acceptance for the various sub-processes and the overall acceptance for the main detector for each period is shown in Table 4.1. For all sub-processes, the change in acceptance between periods is within the error limits. The value of the ratio $\frac{A_{\mathrm{MER}}A_{\mathrm{LER}}}{A^2_{\mathrm{HER}}} = 1.005 \pm 0.012$, indicates that the acceptance correction in Eq. (3.9) can be safely neglected.

process	acceptance		
	HER	MER	LER
elastic	0.2073 ± 0.0053	0.2101 ± 0.0075	0.2064 ± 0.0068
photon dissociation	0.7783 ± 0.0070	0.7807 ± 0.0097	0.7752 ± 0.0089
proton dissociation	0.2753 ± 0.0068	0.2785 ± 0.0094	0.2808 ± 0.0087
double dissociation	0.8063 ± 0.0400	0.8073 ± 0.0561	0.8078 ± 0.0525
resolved	0.8708 ± 0.0057	0.8770 ± 0.0079	0.8752 ± 0.0073
direct	0.9420 ± 0.0107	0.9413 ± 0.0149	0.9376 ± 0.0137
all processes	**0.7644 ± 0.0035**	**0.7673 ± 0.0048**	**0.7652 ± 0.0044**

Table 4.1: The acceptance of the main detector for the various photoproduction sub-processes.

4.5 PCAL + AEROGEL Calibration

The PCAL is the only available tool to estimate and subtract the BH overlaid background events and it was used extensively for this purpose in Sect. 4.6.1. The calibration of the calorimeter part of the LUMI system was done only for the PCAL without the AEROGEL detectors. Therefore, as mentioned in Sect. 2.2.3, the resolution was compromised due to the two carbon absorbers. Thus, an attempt was made to improve the energy resolution and redo the calibration using the AEROGEL detectors.

Initially, the calibration of the AEROGEL detectors was planned to be achieved with the PCAL Monte-Carlo. However, a better approach would be to perform the calibration using data collected by the LUMI system. The following relation was defined for the calibration:

$$E_\gamma = aE_{\mathrm{AERO}_1} + bE_{\mathrm{AERO}_2} + cE_\gamma^{\mathrm{scint}}, \tag{4.2}$$

where E_γ is the energy of the photon, E_{AERO_1} and E_{AERO_2} are the ADC values of the AEROGEL detectors, $E_\gamma^{\mathrm{scint}}$ is the uncalibrated energy of the PCAL and a, b and c are parameters to be determined from the calibration. The value of E_γ was calculated from the assumption that the energy of the photon and the energy of the positron must add up to the energy of the beam,

$$E_\gamma = E_{\mathrm{beam}} - E_{6\mathrm{mT}}. \tag{4.3}$$

To determine the calibration constants a, b and c, a χ^2 minimization method was used:

$$\chi^2 = \sum_{n=1}^{N} \frac{(\sum_{j=1}^{3} \alpha_j e_{j,n} - E_n^\gamma)^2}{\sigma^2_{E_n^\gamma}}, \tag{4.4}$$

where α_j is the parameters vector, e_j is a vector containing the PCAL and AEROGEL energies and N is the number of events. Differentiating yields,

$$\sum_{j=1}^{3} \alpha_j \sum_{n=1}^{N} \frac{e_{j,n} e_{i,n}}{\sigma^2_{E_n^\gamma}} = \sum_{n=1}^{N} \frac{E_n^\gamma e_{i,n}}{\sigma^2_{E_n^\gamma}}. \tag{4.5}$$

The calibration was done separately for the HER, MER and LER. Each period is relatively short; therefore, it is safe to assume that the detector resolution was stable throughout the calibration period. In that case, the uncertainty on the energy of the photon, $\sigma_{E_n^\gamma}$, becomes a constant and can be eliminated from Eq. (4.5)

$$\sum_{j=1}^{3} \alpha_j \sum_{n=1}^{N} e_{j,n} e_{i,n} = \sum_{n=1}^{N} E_n^\gamma e_{i,n}. \tag{4.6}$$

4.5.1 Event selection

A clean BH data sample was needed for the calibration and thus, the selection aimed primarily at high purity of the data sample. The efficiency of the selection was not an issue due to the large data sample available for the calibration.

As mentioned in Sect. 2.2.3, BH photons should deposit energy in both the AEROGEL detectors and in the PCAL. Moreover, the energy deposited in the AEROGEL detector is expected to be correlated with the energy measured in the PCAL. By drawing the ADC values in each AEROGEL as a function of the uncalibrated energy in PCAL (see Fig. 4.15) one can clearly see how the distribution of events is divided into events with real photons depositing energy in both detectors, and events which can only be interpreted as noise or background processes such as synchrotron radiation. Selecting events only in the area marked with curves in Fig. 4.15 assured a sample with clean BH photons.

In order to choose events with a good positron in the 6mT, the cuts mentioned in Sections 4.1.1 and 4.3.1 were applied.

4.5.2 Calibration results

Figures 4.16a, 4.16b and 4.16c show the energy of BH photons in HER, MER and LER, respectively, as measured by the PCAL, with and without the AEROGEL detectors. A vast improvement between the two measurements can be seen. Using the energy measured by the PCAL without the AEROGEL, many events are overestimated, which results in a non-Gaussian energy distribution. The energy distribution measured with the AEROGEL is the expected symmetric Gaussian shape with better resolution.

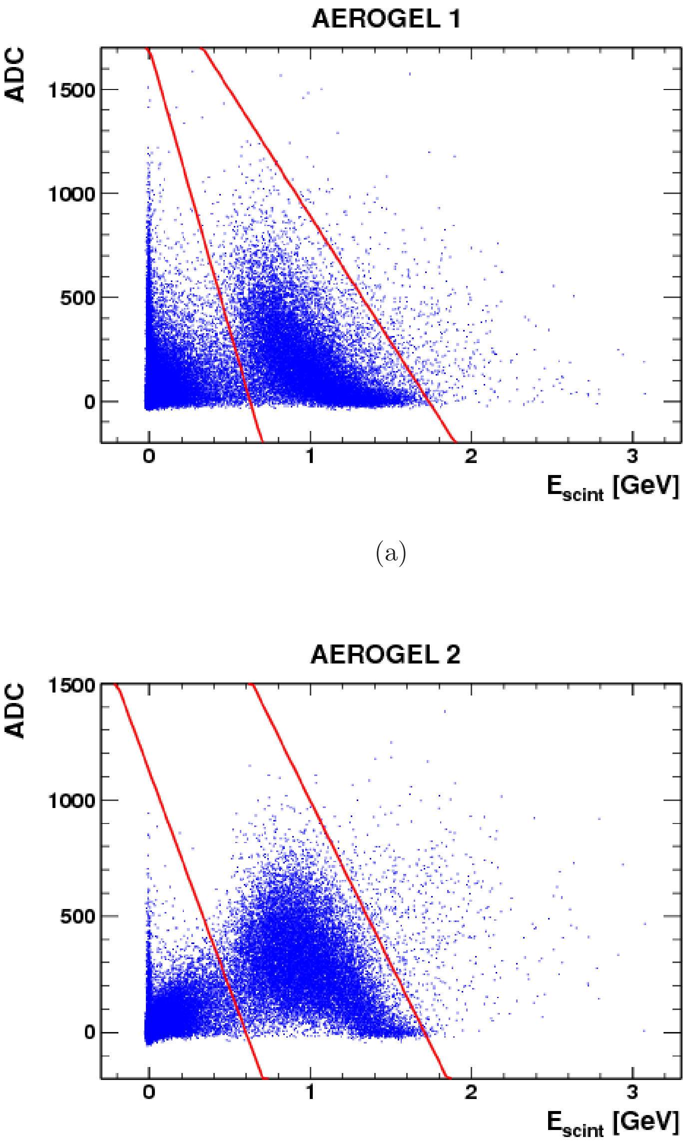

(a)

(b)

Figure 4.15: AEROGEL ADC value as a function of the uncalibrated energy in PCAL, E_{scint}, for (a) first AEROGEL detector and (b) second AEROGEL detector. Only events between the curves were used for the calibration.

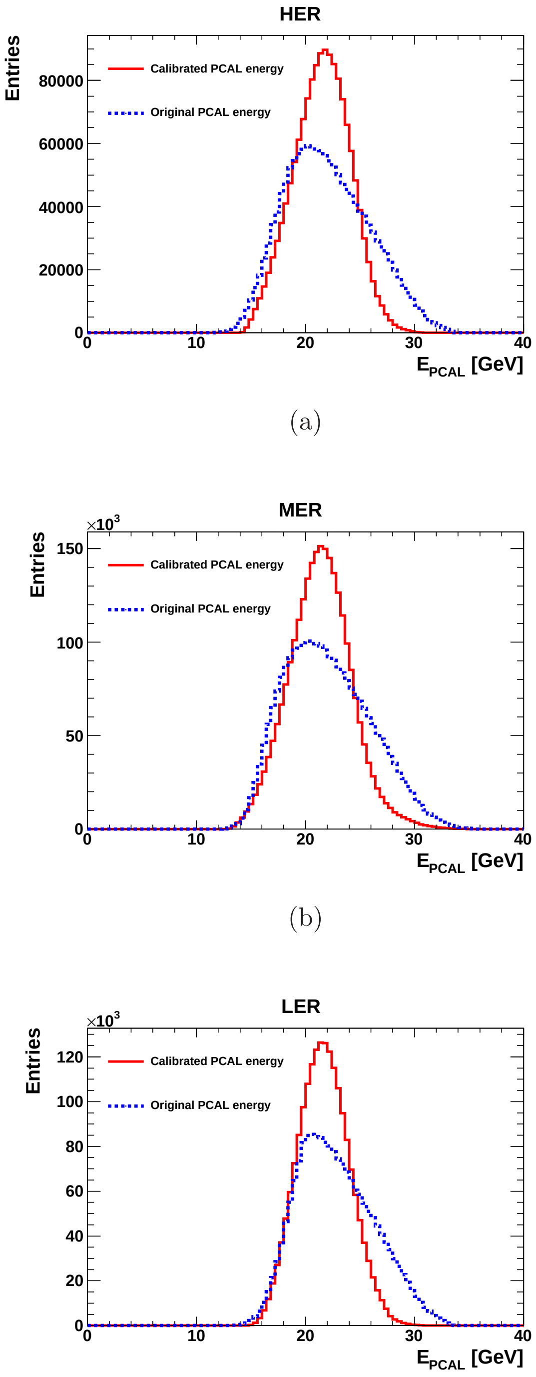

(a)

(b)

(c)

Figure 4.16: Energy measured in the luminosity system, E_{PCAL}, without the AEROGEL detectors (dotted curve) or with the AEROGEL detectors (solid line) in (a) HER, (b) MER and (c) LER.

4.6 Background subtraction

Figure 4.14 clearly shows that some background events remain in the data sample after the cuts depicted in Sect. 4.3. The methods used to estimate the number of such events are discussed in turn.

4.6.1 Bethe-Heitler overlaps

The biggest source of background expected in the data sample are Bethe-Heitler events overlaid with other background events (see Sect. 3.5.1). In BH events, a photon is expected to hit the PCAL. Thus, an investigation of the PCAL energy spectrum of the remaining data sample was required. Figure 4.17a shows the energy in the PCAL, E_{PCAL}, for all events left in the data sample. Figure 4.17b shows E_{PCAL} of events passing an ADC PCAL threshold of $\mathrm{ADC}_{\mathrm{PCAL}} > 1024$ (see next paragraph).
The events seen in the figures may be divided into the following categories:

1. a peak at PCAL energies below 2 GeV - clean photoproduction events;
2. a falling spectrum up to 12 GeV - photoproduction events accompanied by a low energy photon from a BH event;
3. a plateau and falling spectrum from 12 GeV and upwards - BH events along with some other ‘hadronic’ activity in the main calorimeter.

The events in the latter category should be counted and then subtracted from the data sample.

The number of such BH events not rejected by previous cuts may be estimated using data taken by the LUMI data acquisition system during the ZEUS physics runs. Seeing that this is a separate data acquisition system, not correlated with the dedicated trigger for photoproduction events, it can be reliably used for this procedure.
Figure 4.18a displays the E_{PCAL} spectrum of events triggered by the PCAL and collected by the LUMI system. Due to an ADC threshold in the PCAL trigger ($\mathrm{ADC}_{\mathrm{PCAL}} > 1024$), the spectrum is bounded from below at ~ 1.5 GeV. The same threshold was applied while plotting Fig. 4.17b.
This sample of events is composed of photons unassociated with a positron in the 6mT and will therefore be used to estimate the number of events belonging to the 2nd category seen above.

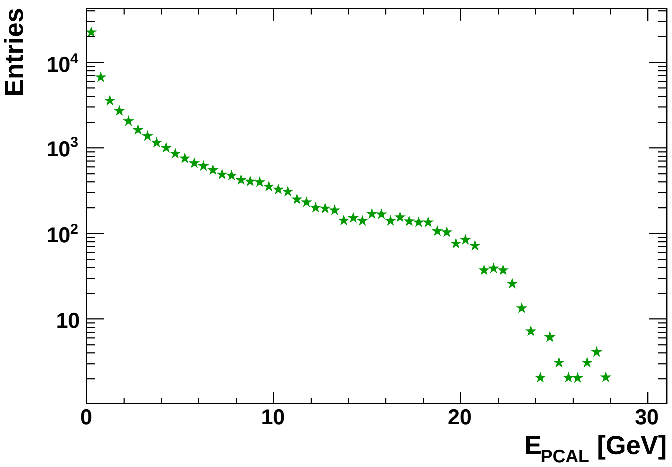

(a)

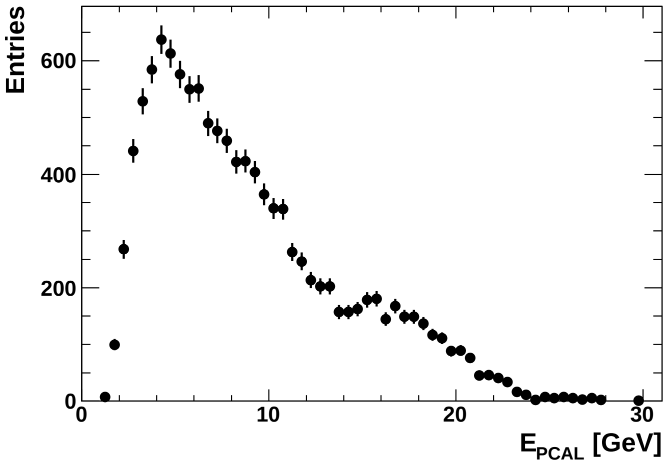

(b)

Figure 4.17: The spectrum of E_{PCAL} for, (a) all events left in the data sample and (b) events above the ADC PCAL threshold of $\mathrm{ADC}_{\mathrm{PCAL}} > 1024$.

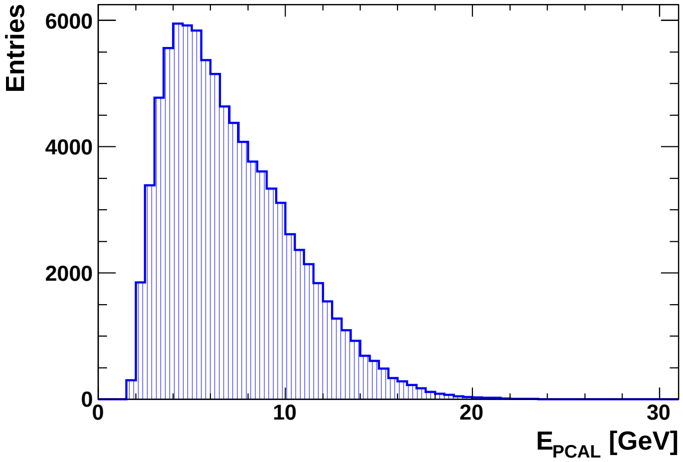

(a)

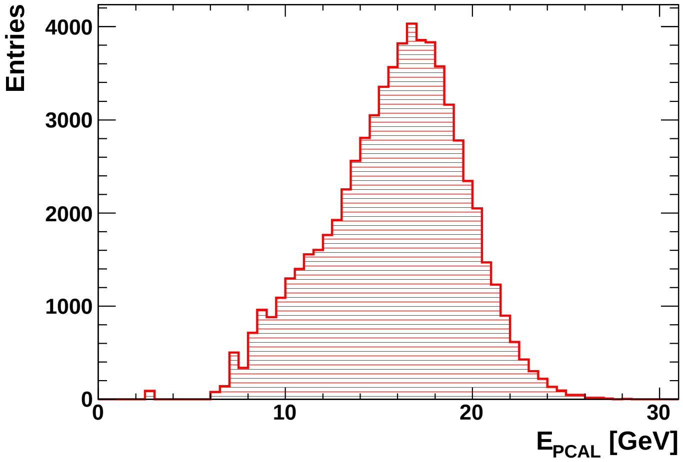

(b)

Figure 4.18: The spectrum of E_{PCAL} for data collected with the LUMI system for, (a) events triggered by the PCAL and (b) events triggered by the 6mT.

By taking events triggered by a positron in the 6mT, one can estimate the number of events which belong to the 3rd category mentioned above. The spectrum of E_{PCAL} for such events is shown in Fig. 4.18b.

Fitting the two histograms presented in Figs. 4.18a and 4.18b to the E_{PCAL} spectrum of the data sample provided in Fig. 4.17b, enables to estimate the number of BH overlay events needed to be subtracted. Figure 4.19 illustrates the process, a fit of the red and blue histograms to the data was used to estimate the contribution of BH overlays.

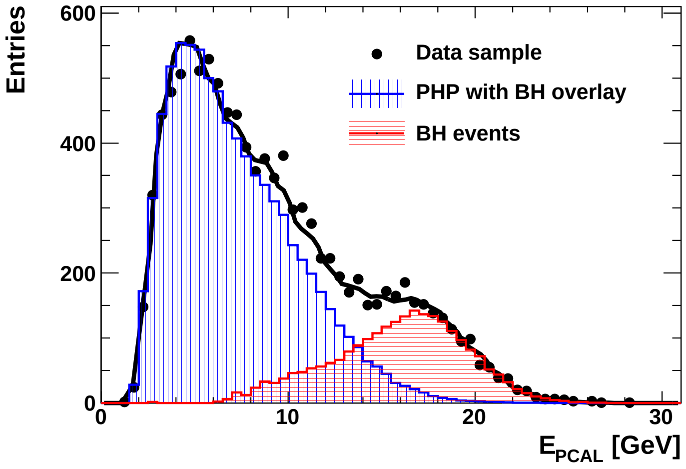

Figure 4.19: The spectrum of E_{PCAL} for: events in the data sample (black dots), events triggered by the PCAL (blue histogram) and events triggered by the 6mT (red histogram). The fit is noted by the black curve.

To get the number of BH overlay events, the number extracted from the fit needs to be multiplied by a factor, s, which takes into account photons lost due to the acceptance of the PCAL and the PCAL veto. The definition of s is as follows:

$$s = 1 + \frac{f}{A_{\text{PCAL}}}(1 - A_{\text{PCAL}}), \tag{4.7}$$

where A_{PCAL} is the acceptance of the PCAL and f accounts for the photons lost by the PCAL veto. The acceptance of the PCAL was given by the

LUMI system [32]. The factor f is determined by the number of events counted without the veto divided by the number of events counted with the veto.

Last but not least, genuine photoproduction events belonging to the 2nd category above, but with BH photons with energy above 14 GeV, were lost due to the PCAL veto. These events must be corrected for. A weight, calculated with a simulation of the LUMI system [32], was given to each event in the data sample accordingly.

This subtraction process was done for each run, HER, MER and LER separately. Figure 4.20 presents the distributions of energy in RCAL after the BH overlap subtraction. The events in the peak at low RCAL energies, seen in the data in Fig. 4.14, were identified as Bethe-Heitler overlaps and subtracted. A better agreement between the data and the Monte-Carlo is seen after the subtraction process.

4.6.2 *e*-gas overlaps

The number of events from e-pilot bunches that were not rejected by previous cuts may be used to evaluate the amount of beam-gas events left in the data sample. The probability to have a beam-gas event in an ep bunch is proportional to the ratio of the number of positrons in a colliding bunch to the number of positrons in an e-pilot bunch, squared [34]. This ratio is equivalent to the ratio of integrated currents. It was calculated per ZEUS run and each e-pilot event was weighted accordingly.
The number of e-pilot events passing the previous cuts was, $N_{e-\mathrm{pilot}} = 6$ in HER, $N_{e-\mathrm{pilot}} = 55$ in MER and $N_{e-\mathrm{pilot}} = 67$ in LER. These numbers correspond, after re-weighting, to the following estimations for beam-gas events in each data sample:

- HER: $N_{e-\mathrm{gas}} = 140$;
- MER: $N_{e-\mathrm{gas}} = 1187$;
- LER: $N_{e-\mathrm{gas}} = 1440$.

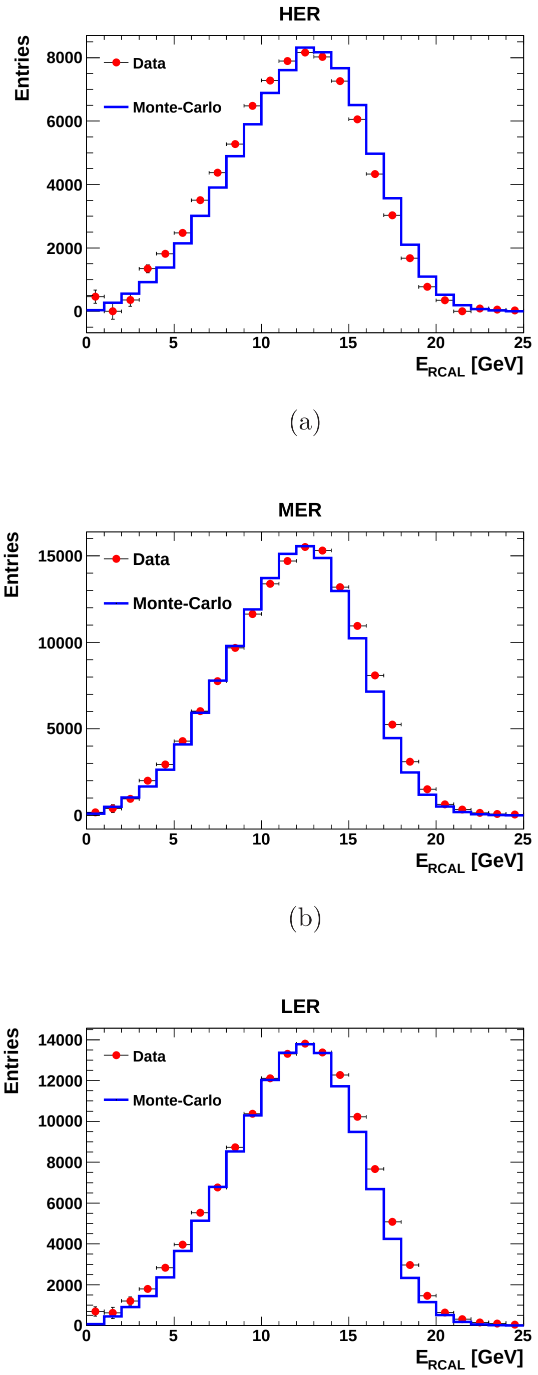

(a)

(b)

(c)

Figure 4.20: Distribution of energy deposited in the RCAL, E_{RCAL}, obtained in the data after BH overlap subtraction (points) and the corresponding distribution expected in the Monte-Carlo (histograms) in (a) HER, (b) MER and (c) LER.

4.7 Systematic studies

In order to check the stability of the measured ratio R, with respect to the cuts applied on the data, the following systematic studies were performed:

- the "splash" cut parameter (0.65) was increased and decreased by 10%, the resulting change in R was $^{+0.0013}_{-0.0042}$;
- the $E(x)$ band cut was widened to $\pm 3.5\sigma_E(x)$, yielding a change in R of 0.0039;
- the $y(x)$ band cut was widened to $\pm 3.5\sigma_y(x)$, the resulting change in R was 0.0090;
- the F_{max} cut curve was shifted to the right and to the left by 10%, the observed changes in R were $^{+0.0048}_{-0.0005}$.

The studies performed on the cuts applied on the 6mT result in changes in the number of events and the ratio R. However, such changes would modify the result for the flux of virtual photons accordingly due to the direct measurement of the flux. Thus, the final result would remain the same. All other changes in R as a result of the systematic studies were well below the statistical uncertainty.

Chapter 5

Results

5.1 Determination of R

Following is a summary of the measured values in each run:

- HER: $N_{d_H} = 76,867 \pm 277$, $\mathcal{L}_{\mathrm{H}} = 566\ \mathrm{nb}^{-1}$, $N_{bg_H} = 3036 \pm 227$,
- MER: $N_{d_M} = 130,983 \pm 362$, $\mathcal{L}_{\mathrm{M}} = 948\ \mathrm{nb}^{-1}$, $N_{bg_M} = 6082 \pm 194$,
- LER: $N_{d_L} = 119,363 \pm 345$, $\mathcal{L}_{\mathrm{L}} = 912\ \mathrm{nb}^{-1}$, $N_{bg_L} = 6230 \pm 230$,

where N_d is the number of events measured after all cuts, $\mathcal{L}$ is the measured luminosity and N_{bg} is the number of background events statistically estimated. The ratio, R, is then given by

$$R = \frac{(N_{d_H} - N_{bg_H})^2}{(N_{d_M} - N_{bg_M}) \cdot (N_{d_L} - N_{bg_L})} \cdot \frac{\mathcal{L}_{\mathrm{M}}\mathcal{L}_{\mathrm{L}}}{\mathcal{L}_{\mathrm{H}}^2}. \tag{5.1}$$

Using the above mentioned numbers, the result for R is

$$R = 1.039 \pm 0.011\ (\text{stat.}) \pm 0.026\ (\text{sys.}).$$

The systematic uncertainty originates from the relative uncertainty on the luminosity and the BH overlap subtraction. Additional sources of systematic uncertainties were explored, but were not included since they were well below the statistical uncertainty.

5.2 Extraction of ϵ

According to Eq. (3.7), the ratio R can be expressed in terms of $\sigma_{\mathrm{tot}}(\gamma p)$ as

$$R = \frac{\int_{y^{\mathrm{H}}_{\mathrm{min}}}^{y^{\mathrm{H}}_{\mathrm{max}}} F_{\mathrm{H}}(y) \left(2\sqrt{E_e E^{\mathrm{H}}_p y}\right)^{\delta} dy \int_{y^{\mathrm{H}}_{\mathrm{min}}}^{y^{\mathrm{H}}_{\mathrm{max}}} F_{\mathrm{H}}(y) \left(2\sqrt{E_e E^{\mathrm{H}}_p y}\right)^{\delta} dy}{\int_{y^{\mathrm{M}}_{\mathrm{min}}}^{y^{\mathrm{M}}_{\mathrm{max}}} F_{\mathrm{M}}(y) \left(2\sqrt{E_e E^{\mathrm{M}}_p y}\right)^{\delta} dy \int_{y^{\mathrm{L}}_{\mathrm{min}}}^{y^{\mathrm{L}}_{\mathrm{max}}} F_{\mathrm{L}}(y) \left(2\sqrt{E_e E^{\mathrm{L}}_p y}\right)^{\delta} dy}, \tag{5.2}$$

where y_{min} and y_{max} are the minimum and maximum detected positron energies, respectively, $F(y)$ is the flux of photons, E_e and E_p are the beam energies of the positrons and protons, respectively, and δ is the power law parameter assumed for the energy dependence. It relates to ϵ via the relation $\delta = 2\epsilon$.

In the measured y range, the value of $\left(2\sqrt{E_e E_p y}\right)^{\delta}$ changes by less than 1%. Therefore, it is possible to replace it with the average value and take it out of the integral,

$$\int_{y_1}^{y_2} F_{\gamma}(y) \left(2\sqrt{E_e E_p y}\right)^{\delta} dy \approx \left(2\sqrt{E_e E_p y_{av}}\right)^{\delta} \int_{y_1}^{y_2} F_{\gamma}(y)\, dy,$$

with the following values for $W_{av} = 2\sqrt{E_e E_p y_{av}}$

- HER: $W_{av} = 285$ GeV;
- MER: $W_{av} = 225$ GeV;
- LER: $W_{av} = 201$ GeV.

The measurement of the integrated flux, $f_{\gamma} = \int_{y_1}^{y_2} F_{\gamma}(y)\, dy$, yielded [30]

- HER: $f_{\gamma} = (8.519 \pm 0.101) \times 10^{-4}$;
- MER: $f_{\gamma} = (8.946 \pm 0.090) \times 10^{-4}$;
- LER: $f_{\gamma} = (8.776 \pm 0.090) \times 10^{-4}$.

The power law parameter, δ, was then determined to be

$$\delta = 0.1990 \pm 0.018 \text{ (stat.)} \pm 0.064 \text{ (sys.)},$$

where the systematic uncertainty includes the uncertainty on the flux. This translates to a Pomeron intercept, $\alpha_{I\!P}(0) = 1 + \epsilon$, with a value of

$$\epsilon = 0.0995 \pm 0.0091 \text{ (stat.)} \pm 0.0321 \text{ (sys.)}.$$

This result is in excellent agreement with earlier determinations of ϵ. However, it has the advantage of being measured directly in a single experiment.

Chapter 6

Summary

The energy dependence of the total γp cross-section was determined using data collected at three different proton beam energies with the ZEUS detector at HERA. Assuming $\sigma_{\rm tot}(\gamma p) \sim W^{\delta}$, the measured value of δ was

$$\delta = 0.1990 \pm 0.018 \text{ (stat.)} \pm 0.064 \text{ (sys.)}.$$

This translates to a Pomeron intercept, $\alpha_{I\!P}(0) = 1 + \epsilon$, with a value of

$$\epsilon = 0.0995 \pm 0.0091 \text{ (stat.)} \pm 0.0321 \text{ (sys.)}.$$

This result is in excellent agreement with earlier determinations of ϵ. However, it has the advantage of being measured directly in a single experiment.

Acknowledgments

First and foremost, I would like to thank my supervisors, Prof. Halina Abramowicz and Prof. Aharon Levy. Thank you for introducing me to the field of high energy physics, for your guidance and help with this analysis and for the personal relationship.

A special thanks also goes to Dr. William Schmidke, who made large contributions to this analysis. Thank you for sharing your knowledge with me and for interesting discussions.

I am grateful to my friends in the Tel Aviv University experimental high energy physics group, Prof. Samuel Dagan, Dr. Sergey Kananov, Ronen Ingbir, Iftach Sadeh, Rina Schwartz and Itamar Levy. I learned a lot from all of you and more importantly, had fun.

A big thank you to Dr. Zhenya Gurvich, whose help on computer related issues has been invaluable.

I am especially grateful to Amir Stern, without your help I could not have started, continued or finished this work.

Finally, I would like to thank my family and my girlfriend, Lucila, for their support, encouragement and patience.

Bibliography

[1] Particle Data Group , L. Montanet *et al. Phys. Rev.*, vol. D 50, p. 1173, 1994.

[2] G. Giacomelli, “Rising total hadron-hadron cross sections,” Tech. Rep. arXiv:0712.0906, Dec 2007. Comments: Talk Festschrift Zatsepin (George T).

[3] ZEUS Collaboration, S. Chekanov *et al. Nucl. Phys.*, vol. B 627, p. 3, 2002.

[4] H1 Collaboration, S. Aid *et al. Zeit. Phys.*, vol. C 69, p. 27, 1995.

[5] A. Donnachie and P. V. Landshoff *Phys. Lett.*, vol. B 296, p. 227, 1992.

[6] J. R. Cudell *et al. Phys. Rev.*, vol. D 61, p. 034019, 2000.

[7] J. R. Cudell, K. Kang, and S. K. Kim *Phys. Lett.*, vol. B 395, p. 311, 1997.

[8] E. Gianfelice Wendt, “HERA upgrade plans.” URL: `epaper.kek.jp/e98/PAPERS/MOX03A.PDF`, 1998.

[9] “The ZEUS Detector.” URL: `http://www-zeus.desy.de/public/zeus.php3`.

[10] ZEUS Collaboration., U. Holm (ed.), “The ZEUS Detector.” Status Report, (unpublished), DESY, available at, URL: `http://www-zeus.desy.de/bluebook/bluebook.html`, 1993.

[11] M. Derrick *et al. Nucl. Instr. and Meth.*, vol. A 309, p. 77, 1991.

[12] N. Harnew *et al. Nucl. Instr. and Meth.*, vol. A 279, p. 290, 1989.

[13] A. Polini *et al. Nucl. Instr. and Meth.*, vol. A 581, p. 656, 2007.

[14] S. D. Paganis *International Journal of Modern Pyhsics*, vol. A 16, p. 1147, 2001.

[15] S. D. Paganis, "A luminosity spectrometer for the zeus experiment at hera," 2000. URL: `arXiv:hep-ph/0604101`.

[16] N. Krumnack, "Testbeam Experiments and Monte Carlo Simulation of the ZEUS 6m Tagger." Dissertation, 2001.

[17] J. Chwastowski *et al. Nucl. Instr. and Meth.*, vol. A 504, p. 222, 2003.

[18] B. Foster, "ZEUS at HERA II," 2001. URL: `arXiv:hep-ex/0107066v1`.

[19] J. Chwastowski *et al.*, "AEROGEL Chernokov Detectors for the Luminosity Measurement at HERA." URL: `http://www-zeus.desy.de/~figiel/posters/poster_v1.pdf`.

[20] M. Schröder, "Calibration of the ZEUS 6m Tagger." Dissertation, DESY-THESIS-2008-039, 2008.

[21] A. Stern, "Measurement of the W dependence of $\sigma_{\text{tot}}(\gamma p)$ with the ZEUS detector at HERA." Dissertation, 2008.

[22] H. A. J. R. Uijterwaal *et al.*, "The ZEUS Central Tracking Detector Second Level Trigger." International Conference on Computing in High Energy Physics, available at, URL: `http://www.hep.net/chep95/html/papers/p16/p16.pdf`, 1995.

[23] T. H. Bauer *et al. Rev. Mod. Phys.*, vol. 50, p. 261, 1978.

[24] G. A. Schuler and T. Sjöstrand *Phys. Lett.*, vol. B 300, p. 169, 1993.

[25] D. Schildknecht, "Vector meson dominance," 2005. URL: `arXiv:hep-ph/0511090v1`.

[26] H. B. O'Connell *et al.*, "Rho-omega mixing, vector meson dominance and the pion form-factor," 1997. URL: `arXiv:hep-ph/9501251v3`.

[27] A. Levy, H. Abramowicz, and W. Schmidke, "Reweighting PYTHIA." Talks given at SFE+QCD work group meeting, available at, URL: `http://www-zeus.desy.de/physics/sfe/ZEUS_ONLY/tools/pytrw/`, 2009.

[28] A. Levy, "Low-x physics at hera," p. 155 p, Feb 1997.

[29] C. F. v. Weizsäcker *Zeit. Phys.*, vol. 88, pp. 612–625, 1934.

E. J. Williams *Phys. Rev.*, vol. 45, no. 10, pp. 729–730, 1934.

[30] W. Schmidke, "6m tagger photon flux measurement with untagged data samples." available at, URL: `http://www-zeus.desy.de/~schmidke/ZEUS_ONLY/sigtot/sigtot.html`, 2010.

[31] W. Schmidke, "σ_{tot} progress report." Talk given at F_L monthly meeting, May 20, available at, URL: `http://www-zeus.desy.de/~schmidke/ZEUS_ONLY/sigtot/sigtot.html`, 2008.

[32] W. Schmidke private communication.

[33] W. Schmidke, "σ_{tot} progress report." Talk given at F_L analysis week, Dec. 5, available at URL: `http://www-zeus.desy.de/~schmidke/ZEUS_ONLY/sigtot/sigtot.html`, 2007.

[34] W. Schmidke, "σ_{tot} progress report." Talk given at F_L meeting, Mar. 13, available at, URL: `http://www-zeus.desy.de/~schmidke/ZEUS_ONLY/sigtot/sigtot.html`, 2008.

תקציר

תלות חתך הפעולה הכולל של אינטרקצית פוטון-פרוטון, $\boldsymbol{\sigma}_{\text{tot}}(\boldsymbol{\gamma p})$, באנרגיית מרכז המסה, $\boldsymbol{W}$, מתוארת באנרגיות גבוהות כחוק חזקה, $\boldsymbol{\sigma}_{\text{tot}}(\boldsymbol{\gamma p}) \sim \boldsymbol{W}^{\boldsymbol{\delta}}$, כאשר $\boldsymbol{\delta} \cong 0.16$.

בעזרת נתונים שנאספו על ידי הגלאי ZEUS במאיץ החלקיקים HERA, מאינטראקציות פוטון-פרוטון בשלושה תחומים שונים של אנרגיות מרכז-מסה, נמצא ערכו של $\boldsymbol{\delta}$:

$$\boldsymbol{\delta} = 0.1990 \pm 0.0182 \text{ (stat.) } \pm 0.0642 \text{ (sys.)}$$

ערך זה מיתרגם לערך נקודת החיתוך של מסלול הפומרון, $\boldsymbol{\alpha}_{\boldsymbol{P}}(0) = 1 + \boldsymbol{\varepsilon}$, כאשר

$$\boldsymbol{\varepsilon} = 0.0995 \pm 0.0091 \text{ (stat.) } \pm 0.0321 \text{ (sys.)}$$

תוצאה זו מתיישבת עם ערכים שנמצאו במדידות קודמות.

אוניברסיטת תל-אביב
הפקולטה למדעים מדויקים
ע"ש ריימונד ובברלי סאקלר

מדידת התלות באנרגיה של חתך הפעולה של אינטראקצית פוטון-פרוטון באמצעות הגלאי ZEUS במאיץ החלקיקים HERA

חיבור זה הוגש כחלק מהדרישות לקבלת
תואר מוסמך M.Sc. באוניברסיטת תל-אביב

ביה"ס לפיזיקה ולאסטרונומיה
החוג לחלקיקים

על-ידי

אוראל גואטה

מאי 2010

העבודה הוכנה בהדרכתם של פרופ' **הלינה אברמוביץ** ופרופ' **אהרן לוי.**